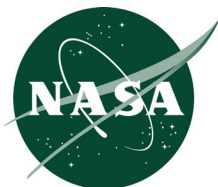NASA/CR—2009–215635

Pulsed Plasma Accelerator Modeling

M. Goodman, F. Kazeminezhad, and T. Owens
The Institute for Scientific Research, Inc., Fairmont, WV 26555

January 2009

The NASA STI Program…in Profile

Since its founding, NASA has been dedicated to the advancement of aeronautics and space science. The NASA Scientific and Technical Information (STI) Program Office plays a key part in helping NASA maintain this important role.

The NASA STI program operates under the auspices of the Agency Chief Information Officer. It collects, organizes, provides for archiving, and disseminates NASA's STI. The NASA STI program provides access to the NASA Aeronautics and Space Database and its public interface, the NASA Technical Report Server, thus providing one of the largest collections of aeronautical and space science STI in the world. Results are published in both non-NASA channels and by NASA in the NASA STI Report Series, which includes the following report types:

- TECHNICAL PUBLICATION. Reports of completed research or a major significant phase of research that present the results of NASA programs and include extensive data or theoretical analysis. Includes compilations of significant scientific and technical data and information deemed to be of continuing reference value. NASA's counterpart of peer-reviewed formal professional papers but has less stringent limitations on manuscript length and extent of graphic presentations.

- TECHNICAL MEMORANDUM. Scientific and technical findings that are preliminary or of specialized interest, e.g., quick release reports, working papers, and bibliographies that contain minimal annotation. Does not contain extensive analysis.

- CONTRACTOR REPORT. Scientific and technical findings by NASA-sponsored contractors and grantees.

- CONFERENCE PUBLICATION. Collected papers from scientific and technical conferences, symposia, seminars, or other meetings sponsored or cosponsored by NASA.

- SPECIAL PUBLICATION. Scientific, technical, or historical information from NASA programs, projects, and missions, often concerned with subjects having substantial public interest.

- TECHNICAL TRANSLATION. English-language translations of foreign scientific and technical material pertinent to NASA's mission.

Specialized services also include creating custom thesauri, building customized databases, and organizing and publishing research results.

For more information about the NASA STI program, see the following:

- Access the NASA STI program home page at <http://www.sti.nasa.gov>

- E-mail your question via the Internet to <help@sti.nasa.gov>

- Fax your question to the NASA STI Help Desk at 443–757–5803

- Phone the NASA STI Help Desk at 443–757–5802

- Write to:
  NASA STI Help Desk
  NASA Center for AeroSpace Information
  7115 Standard Drive
  Hanover, MD 21076–1320
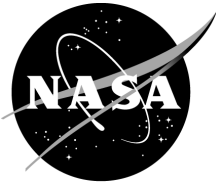
Pulsed Plasma Accelerator Modeling

M. Goodman, F. Kazeminezhad, and T. Owens
The Institute for Scientific Research, Inc., Fairmont, WV 26555

National Aeronautics and
Space Administration

Marshall Space Flight Center • MSFC, Alabama 35812

January 2009

Acknowledgments

TABLE OF CONTENTS

LIST OF FIGURES

Abstract

This report presents the main results of the modeling task of the PPA project. The objective of this task is to make major progress towards developing a new computational tool with new capabilities for simulating cylindrically symmetric 2.5 dimensional (2.5 D) PPA's. This tool may be used for designing, optimizing, and understanding the operation of PPA's and other pulsed power devices. The foundation for this task is the 2 D, cylindrically symmetric, magnetohydrodynamic (MHD) code PCAPPS (Princeton Code for Advanced Plasma Propulsion Simulation). PCAPPS was originally developed by Sankaran (2001, 2005) to model Lithium Lorentz Force Accelerators (LLFA's), which are electrode based devices, and are typically operated in continuous mode. The magnetic field in this code only has an azimuthal component. For the PPA project, PCAPPS was modified to apply to PPA's, which are drive coil based devices operated in pulsed mode. The modification consists of changing the geometry of the computational domain, adding the radial component of the magnetic field to the model, and implementing a first principles, self-consistent algorithm to couple the plasma and power circuit that drives the plasma dynamics. This coupling algorithm is the most important result of the modeling effort so far. As in reality, the coupling occurs through the current and electric field in the drive coil. At a given time t the current in the drive coil provides a boundary condition for PCAPPS, allowing the code to be advanced to the next time step $t + \Delta t$. Then the voltage drop $V_{plasma}(t + \Delta t)$ across the drive coil due to the plasma electric field is computed and represented in the power circuit equations as an EMF in series with the drive coil's resistance and inductance. The plasma electric field is computed from the Ohm's law used in PCAPPS, and includes all effects of the plasma dynamics on the power circuit. The voltage drop across the drive coil is V_{plasma} plus the voltage drops across the drive coil's resistance and inductance. The power circuit equations are then solved to determine the drive coil current at time $t + \Delta t$, which provides an updated boundary condition for PCAPPS. This iterative algorithm is applied at each time step. The coupling algorithm appears to be new. It is general in that it allows any Ohm's law, and any power circuit that couples to the plasma through a drive coil to be included in any PPA simulation. The basic structure of PCAPPS, including these modifications, is described. Simulations of pulsed inductive thrusters (PIT's) having drive coil radii of 5.5 cm and 13.5 cm, and for Lithium and Argon propellants are presented. For these simulations, the thruster is powered by a capacitor in an LRC circuit using values of L,R, and C characteristic of TRW PIT thruster experiments. The objective of the modeling task was achieved in that: (1) An apparently new, self consistent, general, first principles based power circuit-plasma coupling algorithm was conceived and implemented; (2) Major modifications were successfully made to PCAPPS as part of the longer range objective to make the code fully 2.5 D.

1.0 The Model

PCAPPS is a two dimensional, cylindrically symmetric MHD code. Cylindrical coordinates (r, θ, z) are used. z is the coordinate along the axis of the cylinder, r is the distance from the cylinder axis, and all quantities are independent of θ. The drive coil is a disk in the plane $z = 0$. Its axis is the z axis, and the direction of increasing z is away from the drive coil. PCAPPS contains a description of the transport processes currently believed to be most important for the description of PPA's. It contains the parallel (Spitzer) and Hall electrical conductivities, an expression for anomalous resistivity, scalar expressions for the electron and ion thermal conductivities, and a semi-empirical expression for radiative loss.

The conservation equations for the total mass, momentum, and energy, and Faraday's law are:

$$\frac{\partial (r\rho)}{\partial t} + \frac{(r\rho u)}{\partial r} + \frac{\partial (r\rho w)}{\partial z} = 0 \tag{1}$$

$$\frac{\partial (r\rho u)}{\partial t} + \frac{\partial \left[r \left(\rho u^2 + \frac{B_\theta^2}{2\mu_0} + p \right) \right]}{\partial r} + \frac{\partial (r\rho u w)}{\partial z} = p - \frac{B_\theta^2}{2\mu_0} \tag{2}$$

$$\frac{\partial (r\rho w)}{\partial t} + \frac{\partial (r\rho u w)}{\partial r} + \frac{\partial}{\partial z} \left[r \left(\rho w^2 + p + \frac{B_\theta^2 + B_r^2}{2\mu_0} \right) \right] = 0 \tag{3}$$

$$\frac{\partial B_\theta}{\partial t} + \frac{\partial}{\partial r} \left(u B_\theta - \eta j_z - \frac{j_r B_\theta - j_\theta B_r}{n_i e} \right) + \frac{\partial}{\partial z} \left(w B_\theta + \eta j_r - \frac{j_z B_\theta}{n_i e} \right) = 0 \tag{4}$$

$$\frac{\partial B_r}{\partial t} + \frac{\partial}{\partial z} \left(w B_r - \eta j_\theta - \frac{j_z B_r}{n_i e} \right) = 0 \tag{5}$$

$$\frac{\partial (r\varepsilon)}{\partial t} + \frac{\partial}{\partial r} \left\{ r u \left(\varepsilon - \frac{B_r^2 - B_\theta^2}{2\mu_0} + p \right) - \frac{r B_\theta}{\mu_0} \left[\eta j_z + \frac{j_r B_\theta - j_\theta B_r}{e n_i} \right] - r \left[\kappa_{th,e} \frac{\partial T_e}{\partial r} + \kappa_{th,i} \frac{\partial T_i}{\partial r} \right] \right\}$$
$$+ \frac{\partial}{\partial z} \left\{ r w \left(\varepsilon + \frac{B_\theta^2 + B_r^2}{2\mu_0} + p \right) - \frac{r B_\theta}{\mu_0} \left[-\eta j_r + \frac{B_\theta j_z}{e n_i} \right] - \frac{r B_r}{\mu_0} \left[\eta j_\theta + \frac{B_r j_z}{e n_i} \right] - r \left[\kappa_{th,e} \frac{\partial T_e}{\partial z} + \kappa_{th,i} \frac{\partial T_i}{\partial z} \right] \right\}$$
$$+ n_e n_i L (T_e) = 0. \tag{6}$$

Here u and w are the radial and axial components of the velocity; B_θ and B_r are the azimuthal and radial components of the magnetic field; j_r, j_z, and j_θ are the components of the current density; ρ and p are the total mass density and total pressure; T_e and T_i are the electron and ion temperatures; n_e and n_i are the electron and total ion number densities; η is the sum of the Spitzer and anomalous resistivities; and e is the magnitude of the electron charge. Equations (4) and (5) are the nonzero components of Faraday's law. The terms in these equations that are $\propto (e n_i)^{-1}$ are the Hall terms arising from the Hall conductivity[1]. $\kappa_{th,e}$ and $\kappa_{th,i}$ are the electron and ion thermal conductivities. μ_0 is the magnetic permeability

---

[1]The exact Hall terms have n_e in place of n_i. The exact relation between the two is the quasi-neutrality condition $n_e = \sum_{j=1}^{N} j n_i^j$, where the sum is over all ionization stages, and n_i^j is the number density of j times ionized ions. Then the approximation $n_e \sim n_i \equiv \sum_{j=0}^{N} n_i^j$ is justified if the ionization occurs on time scales much shorter than those of interest, and if j is not much larger than unity, which appears to be the case. The reason for making the approximation is to avoid the very small computational time steps that result from $n_e \ll n_i \sim n_i^0$ at the beginning of the simulation before significant ionization occurs. One of the

of vacuum. γ is the ratio of specific heats for the gas of ions and electrons, and is given empirically as a function of T_i in PCAPPS. The term $n_e n_i L(T_e)$ describes radiative energy loss, where $L(T_e)$ is an empirically determined function. $\varepsilon = \frac{1}{2}\rho (u^2 + w^2) + \frac{B_\theta^2 + B_r^2}{2\mu_0} + \frac{p}{\gamma - 1}$ is the total energy density per unit volume. γ is obtained from a model developed by Choueiri [3] that is valid for Lithium and Argon. The anomalous component of the total resistivity η, due to microinstabilities, is derived by Choueiri [4]. The empirical function $L(T_e)$ that occurs in the radiative loss term in the energy equation (6) is given by Post et al. [5] for a Lithium plasma. This function is also used in PCAPPS to describe radiative loss in Argon. It is found by Sankaran (2005) that radiative loss is not a significant cooling mechanism for LLFA plasmas. The same is true for the PPA plasmas considered here since they are characterized by similar temperature and density ranges.

The terms involving B_r and j_θ in equations (1) - (6) are not in the original version of PCAPPS. They are implemented here to extend the capability of PCAPPS to modeling PPA's. As in the original version of PCAPPS, the θ component of the momentum equation, and all terms involving B_z are not included in the model. The extension of PCAPPS presented here is the simplest one that allows for modeling PPA's. An extension of PCAPPS to allow for modeling general 2.5 D, cylindrically symmetric plasma dynamics must include the θ component of the momentum equation, and all terms involving B_z. PCAPPS will be modified to include this equation and these terms in the second phase of the project during 2006 - 2007.

A simple analysis was done to estimate the error involved in omitting the θ component of the momentum equation, and the terms involving B_z when modeling PIT type devices. This analysis and its results are described as follows. The azimuthal component of the momentum equation may be written as $dv/dt = (\mathbf{j} \times \mathbf{B})_\theta \equiv F_\theta$, where dv/dt is the convective (Lagrangian) time derivative of the azimuthal component v of the velocity. Similarly, the other components of the momentum equation may be written as $du/dt = (\mathbf{j} \times \mathbf{B})_r - \partial p/\partial r \equiv F_r$, $dw/dt = (\mathbf{j} \times \mathbf{B})_z - \partial p/\partial z \equiv F_z$. For a typical simulation of a PIT, described later in this report, it is found that $|F_\theta| \sim |F_r| \stackrel{<}{\sim} 10^{-3}|F_z|$ at time $t = 1.41$ μ sec when the current in the power circuit reaches its first peak, and $|F_\theta| \sim (10^{-2} - 10^{-1})|F_r| \sim |F_z|$ at $t = 7.25$ μ sec when the current in the power circuit reaches its second peak. This inequality is maintained for the remainder of the simulation. These results suggest that if the azimuthal component of the momentum equation is included in the model, only a relatively small azimuthal flow speed is generated, in which case the error in omitting this equation is small. The error in omitting terms containing B_z is estimated by using the axial component of Faraday's law, given by $\partial B_z/\partial t = -(\nabla \times \mathbf{E})_z$, with $\mathbf{E}$ given by the Ohm's law of the model. For the same PIT simulation, $\nabla \times \mathbf{E}$ is computed, and its r, θ, and z components are compared. The result is that $|(\nabla \times \mathbf{E})_z| \sim 10^{-1}|(\nabla \times \mathbf{E})_\theta| \sim |(\nabla \times \mathbf{E})_r|$ at $t = 1.41$ μ sec, and $|(\nabla \times \mathbf{E})_z| \sim |(\nabla \times \mathbf{E})_\theta| \sim (10^{-2} - 10^{-1})|(\nabla \times \mathbf{E})_r|$ at $t = 7.25$ μ sec. These results suggest that for a PIT type device the effects of B_z are small compared with those of B_r, but may be comparable with those of B_θ. This is consistent with experimental results for the TRW PIT showing that almost no axial magnetic field is generated during device operation [6, 7].

---

tasks of the follow on phase of the PPA project is to explore the error introduced by this approximation, and compare PCAPPS and MACH2 with respect to how they treat the Hall terms, which can have important effects in 2 and 3 dimensions.

Equations (1)-(6) must be supplemented by additional equations to complete the model. These equations are the electron energy equation, the ideal gas equations of state for the electrons and ions, the caloric equation of state for the electrons, and Saha's equation relating the number densities of electrons and the several ionization stages of the ions.

The electron energy equation is given by

$$
\frac{\partial \varepsilon_e}{\partial t} + \frac{1}{r}\frac{\partial}{\partial r}\left(r\varepsilon_e u\right) + \frac{\partial}{\partial z}\left(\varepsilon_e w\right) + p_e \left(\frac{1}{r}\frac{\partial (ru)}{\partial r} + \frac{\partial w}{\partial z}\right)
$$
$$
= \eta \left(j_r^2 + j_z^2 + j_\theta^2\right) - \frac{3n_e m_e \nu_{ei}}{M_i} \kappa_B \left(T_e - T_i\right) + \nabla \cdot \left(\kappa_{th,e}\nabla T_e\right). \tag{7}
$$

Here $\varepsilon_e, p_e, m_e, M_i, k_B$, and ν_{ei} are the electron energy density per unit volume, electron pressure, electron mass, ion mass, Boltzmann's constant, and the electron-ion collision frequency. The first, second, and third terms on the right hand side of equation (7) correspond to Ohmic heating, electron-ion energy exchange via collisions, and electron heat flux.

The ideal gas and caloric equations of state for the electrons are

$$
T_e = \frac{(\gamma_e - 1)\,\varepsilon_e}{n_e \kappa_B} = \frac{p_e}{n_e \kappa_B}. \tag{8}
$$

Here $\gamma_e = 5/3$.

Saha's equation is

$$
\frac{n_i^j n_e}{n_i^{j-1}} = \frac{2\left(2\pi m_e \kappa_B T_e\right)^{3/2}}{h^3} \frac{\sum_l g_l^j e^{-\varepsilon_l^j/\kappa_B T_e}}{\sum_l g_l^{j-1} e^{-\varepsilon_l^{j-1}/\kappa_B T_e}}. \tag{9}
$$

Here j and $j-1$ label ionization stages, l labels discrete atomic energy levels, and g_l is the statistical weight of the corresponding energy level for a given ionization stage. The use of this Saha equation is based on the assumptions that the distribution of the ions over their internal energy levels (bound and continuum (ionized)) is determined entirely by electron-ion collisions, that this distribution is an equilibrium (Boltzmann) distribution, that the electrons are in equilibrium at temperature T_e, and that the distribution of the ions over their internal energy levels is in equilibrium with the electrons. The electrons and ions are assumed to respond instantaneously on MHD and radiative time scales to maintain these equilibrium conditions. A discussion of the conditions under which these assumptions are valid is given in Sankaran (2001,2005) and references therein. Roughly, the assumptions are valid if $\tau_{ee} \ll \tau_{ei} \ll$ MHD and radiative transition time scales. Here τ_{ee} and τ_{ei} are the electron-electron and electron-ion collision times.

The ion pressure, and equation of state are

$$
p_i = p - p_e \tag{10}
$$
$$
T_i = \frac{p_i}{n_i \kappa_B} \tag{11}
$$

Complete details of the original PCAPPS model and code, including a discussion of the various approximations, are given by Sankaran (2001, 2005).

1.1 Power Circuit - Plasma Coupling Algorithm

One of the most challenging problems in modeling any inductive electric thruster is to model the coupling between the power circuit and plasma with sufficient accuracy. This problem demands a self consistent treatment for an accurate solution since the power circuit-plasma coupling is strongly bi-directional. The inductive electric field generated by the power circuit ionizes and accelerates the propellant. The resulting plasma dynamics generates its own electric field that reacts back on the power circuit, effectively having inductive and resistive effects on the circuit.

Thus far, there have been two basic approaches to modeling the power circuit - plasma coupling. One approach is to treat the plasma as an LRC circuit inductively coupled to the power circuit [6], [7]. This approach includes bi-directional coupling, but the effect of the complex plasma dynamics on the power circuit is treated approximately in terms of lumped circuit elements. The second approach is to drive the plasma with an experimentally determined drive coil current waveform [8]. Mikellides and Neilly perform MACH2 simulations of a PIT driven by such a waveform. This waveform is used to determine $L, R,$ and C in the equivalent LRC circuit that reproduces the current waveform. This approach, though based on measurements of the current in an operating PIT, is uni-directional, and includes all effects of the power circuit and the plasma dynamics together through the values of $L, R,$ and C. These restrictions of uni-directional coupling and lumped element circuit modeling of the effects of plasma dynamics are significant, indicating the need for a bi-directional coupling algorithm that includes the exact plasma dynamics.

Here a simple, self consistent, first principles based algorithm for including the bi-directional power circuit-plasma coupling in PPA simulations is presented and implemented. The algorithm is as follows. The effect of plasma dynamics on the power circuit must occur through the plasma electric field $\mathbf{E}$ acting on the charges in the drive coil. The effect of $\mathbf{E}$ is to alter the voltage V_d between the terminals of the drive coil from what it is in the absence of the plasma. The contribution V_{plasma} of $\mathbf{E}$ to V_d is exactly computed as the scalar line integral of $\mathbf{E}$ along the wires between the terminals of the drive coil. V_{plasma} is then included as an EMF in series with the drive coil resistance and inductance in the circuit equations governing the time evolution of the current through the drive coil in the power circuit. Given V_{plasma} at time t, the current $I(t + \Delta t)$ in the drive coil is computed by solving these equations. $I(t + \Delta t)$ is then used to determine an updated current density at the surface of the drive coil, which provides an updated boundary condition for PCAPPS. This iterative procedure is performed at each time step. $\mathbf{E}$ contains all effects of the plasma dynamics on the power circuit, including time dependent resistive and inductive effects, regardless of the complexity of the plasma dynamics. V_d equals the sum of V_{plasma} and the voltage drops across the R and L in the power circuit that represent the drive coil's resistance and inductance, which may be measured, and are independent of time.

For an arbitrary power circuit the algorithm is easily implemented using a circuit modeling software package such as PSPICE. The drive coil is represented in any power circuit as a constant inductance and resistance, and a time dependent V_{plasma}, all in series. The algorithm iterates between PSPICE and PCAPPS as described above, with PSPICE providing an updated drive coil current boundary condition for PCAPPS, and PCAPPS providing V_{plasma} at each time for PSPICE to compute a new drive coil current.

4

Additional insight into the coupling algorithm is gained by using the electromagnetic boundary condition which states that the tangential component of the total electric field is continuous across any material interface in its rest frame. Let E_{wire} be the electric field that drives and is parallel to the current in the drive coil. Let E_p be the component of the plasma electric field at the surface of, and parallel to the drive coil wires. The boundary condition requires that $E_{wire} = E_p + E'$, where E' is the electric field at the boundary between the wires and the plasma volume that contains the effects of the drive coil's constant resistance and inductance on V_d. The scalar line integral of E' along the wires between the terminals of the drive coil equals the voltage drop across the drive coil due to this resistance and inductance.

For the simulations presented in this report the power circuit is an LRC circuit. The values of L, R, and C, and other simulation parameters are presented in §3.2. Fig. 1 is a schematic diagram of the power circuit-drive coil configuration. The drive coil is shown as a set of concentric wire rings. The axis of the rings is the z axis of the simulation, the drive coil occupies the area defined by ($z = 0, 0 \leq r \leq R_{coil}$), and the wires run along the θ direction. This approximation derives from the design of the original TRW PIT drive coil, which is comprised of 18 spiral strands of wire that can be accurately approximated as 9 concentric wire rings, each carrying an azimuthal current I. For the simulations, the drive coil is assumed to be a continuous disk carrying a uniform (r independent), azimuthal current density j_θ given by

$$j_\theta = \frac{I}{A}, \tag{12}$$

where A is the part of the cross sectional area of each wire in the drive coil through which current flows. It is given by

$$A = \pi R_w^2 - \pi \left(R_w - \delta\right)^2, \tag{13}$$

where R_w is a characteristic radius of a wire strand ($R_w \sim 1$ cm), and δ is the skin depth of copper at the natural frequency of the LRC circuit uncoupled from the plasma. Then the current density at each of the guard cells in the simulation domain along the drive coil radius $0 \leq r \leq R_{coil}$ at $z = 0$ is assigned the value j_θ. j_θ is updated at each time step, and provides the MHD boundary condition at the drive coil that allows PCAPPS to compute the state of the plasma at the next time step.

The circuit equations for the power circuit - plasma system are:

$$V = RI + L\frac{dI}{dt} + V_{plasma} \tag{14}$$

$$Q = CV \tag{15}$$

$$\frac{dQ}{dt} = -I \tag{16}$$

where V is the voltage across the capacitor, and V_{plasma} is obtained from:

$$V_{plasma}(t) = \int_{R_{outer}}^{0} \vec{E} \cdot \vec{dl} = 2\pi \sum_{i=1}^{N} R_i E_\theta(R_i, t). \tag{17}$$

Here E_θ is the component of the plasma electric field at, and parallel to the drive coil wire rings, R_i is the radius of guard cell i from the z axis, and N is the number of guard cells
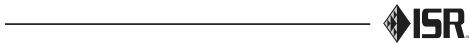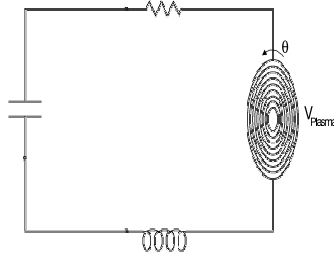
Figure 1: Schematic of the Power Circuit - Plasma System

along the radial direction. E_θ is computed using the PCAPPS Ohm's law as

$$E_\theta = \left(-\mathbf{v} \times \vec{B} + \eta \mathbf{j} + \frac{\mathbf{j} \times \mathbf{B}}{ne} \right)_\theta . \tag{18}$$

The terms on the right hand side of this equation are the convective, resistive, and Hall contributions to E_θ. They are updated at each time step.

The capacitor voltage V, and circuit current I are updated by solving equations (14) - (16). The solution to these equations is

$$
\begin{aligned}
V(t) &= e^{-\lambda t} V_0 \left[\frac{\lambda}{\omega} \sin(\omega t) + \cos(\omega t) \right] \\
&+ \frac{e^{-\lambda t} \sin(\omega t)}{\omega L C} \int_0^t e^{\lambda t'} (V_{plasma}(t')) \cos(\omega t') \, dt' \\
&- \frac{e^{-\lambda t} \cos(\omega t)}{\omega L C} \int_0^t e^{\lambda t'} (V_{plasma}(t')) \sin(\omega t') \, dt' \\
I(t) &= C V_0 e^{-\lambda t} \left[-\frac{\lambda^2 + \omega^2}{\omega} \sin(\omega t) \right] \\
&+ \frac{e^{-\lambda t} (-\lambda \sin(\omega t) + \omega \cos(\omega t))}{\omega L} \int_0^t e^{\lambda t'} (V_{plasma}(t')) \cos(\omega t') \, dt' \\
&+ \frac{e^{-\lambda t} (\lambda \cos(\omega t) + \omega \sin(\omega t))}{\omega L} \int_0^t e^{\lambda t'} (V_{plasma}(t')) \sin(\omega t') \, dt',
\end{aligned}
$$

(19)

(20)

where

$$\omega = \sqrt{\frac{1}{LC} - \left(\frac{R}{2L} \right)^2} \quad \text{and} \quad \lambda = \frac{R}{2L} . \tag{21}$$

I determines the current density at the drive coil that is used as a boundary condition for PCAPPS. The initial conditions $I(0) = 0, V(0) = V_0$ are assumed. PCAPPS is initialized

6

for its first time step by computing dI/dt at $t = 0$, and multiplying the result by a seed time step Δt_s to obtain the required drive coil current boundary condition. For the simulations presented in §3 the choice $\Delta t_s = 5 \times 10^{-9}$ sec is made. The Courant condition then modifies this time step, if necessary, and determines all subsequent time steps. A flow chart of the power circuit - plasma coupling algorithm is shown in Fig. 2.

2.0 Numerical Algorithm

The model uses a characteristic splitting finite volume method. In this method, in each cell j, each fluid equation reduces to

$$\frac{\partial u_j}{\partial t} = -\frac{1}{\Omega_j} \oint \vec{F} \cdot \vec{dl} + < S >_j .$$

(22)

Here Ω_j is the cell volume (area in 2D), the line integral is around the boundary of cell j, u_j is a typical conserved variable (e.g. ρ), $\mathbf{F}$ is the corresponding flux, and $< S >_j$ is the average of the source term, when present, over Ω_j.

There exists a large literature on finite volume methods. For a comprehensive, thorough treatment see Godlewski & Raviart [9]. These methods have emerged as powerful methods in hydrodynamics and MHD since they employ semi-analytic techniques that allow for the resolution of strong discontinuities without the use of filtering schemes such as flux-corrected transport (FCT). Equation (22) is obtained by multiplying each fluid equation by a trial function, and integrating over all space. Here, and in most cases, the trial function is chosen to have unit value in a given cell j, and be zero otherwise. Then the integration over all space reduces the calculations to those involving a single cell j and its boundaries, as indicated in equation (22). Analytic calculations are then employed to determine the values of u_j at cell boundaries in terms of its values at cell centers using a method developed by Roe [10]. This method is based on the analytic Rankine-Hugoniot jump conditions.

The following example shows the effectiveness of the Roe method in resolving strong discontinuities, and serves as a test case for validating the modification of PCAPPS. This example consists of triggering a fast MHD shock wave by using a step function in B_r as an initial condition, and then checking the degree to which the Rankine-Hugoniot jump conditions across the shock front are satisfied. This step function is a change in B_r from 500 to 100 G at the drive coil. It models pulsing a PIT type device with a very short current rise time. A shock wave develops as expected, with all profiles steepening into discontinuities that travel together at the same speed. The Rankine Hugoniot jump condition for each profile is checked. For B_r this condition is obtained from the Faraday law equation (5), and is given by

$$s\Delta B_r = \Delta F_z.$$

(23)

Here s is the shock speed, determined from the speed of the discontinuity in the simulation, and ΔB_r and ΔF_z are the change of B_r and its flux across the discontinuity. The Rankine-Hugoniot conditions are found to be satisfied to within an error $\sim 15\%$. This error is considered small since the simulation is 2 D while the Rankine-Hugoniot jump conditions are derived for a 1 D system.

$$\boxed{\text{Initialization}}$$

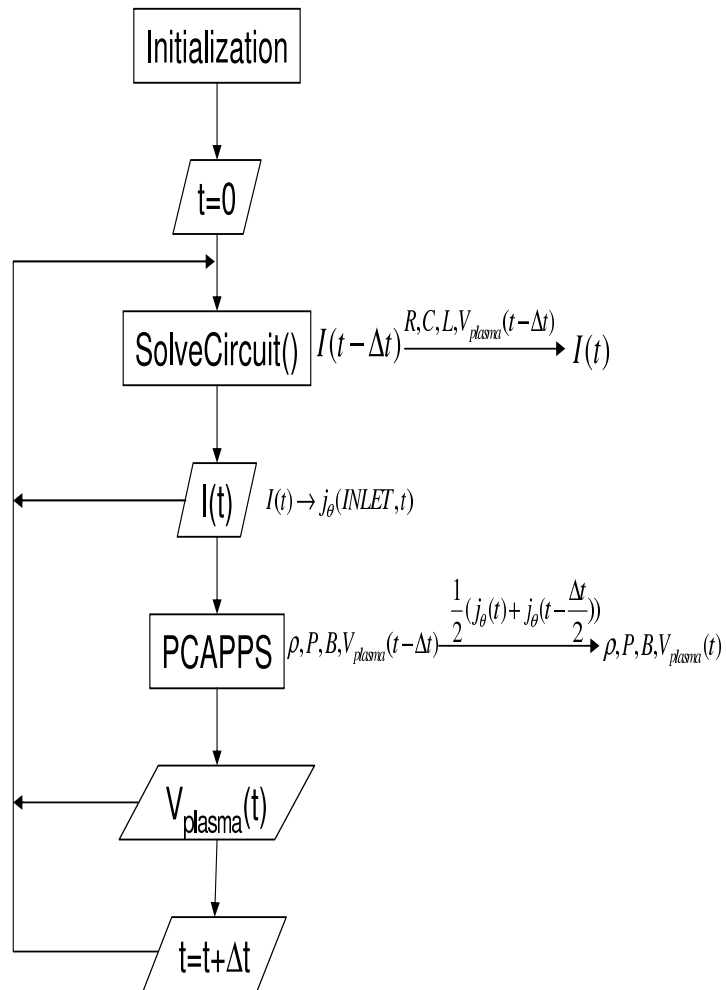$$t=0$$

$$\boxed{\text{SolveCircuit()}} \quad I(t-\Delta t) \xrightarrow{R,C,L,V_{plasma}(t-\Delta t)} I(t)$$

$$I(t) \quad I(t) \rightarrow j_{\theta}(INLET,t)$$

$$\boxed{\text{PCAPPS}} \quad \rho,P,B,V_{plasma}(t-\Delta t) \xrightarrow{\frac{1}{2}(j_{\theta}(t)+j_{\theta}(t-\frac{\Delta t}{2}))} \rho,P,B,V_{plasma}(t)$$

$$V_{plasma}(t)$$

$$t=t+\Delta t$$

Figure 2: Flow Chart of the Power Circuit - Plasma Coupling Algorithm.

An additional test of the code modification of adding B_r to the model is to check the coupling of B_r and B_θ by the Hall electrical conductivity. The test consisted of initializing B_r as a sine wave, and then checking that a corresponding B_θ is generated as a sine wave. This was found to be the case. The two sine waves have approximately the same amplitude in the absence of the plasma resistivity η, as expected.

3.0 Examples of Simulations of Pulsed Plasma Accelerators

3.1   Geometry

The original version of PCAPPS uses a mesh of quadrilaterals to fit an LLFA geometry based on the device design by Polk [11]. Here the geometry is modified to that of a PIT. The radius R_{coil} of the drive coil is chosen to be 5.5 cm or 13.75 cm. The first value corresponds to a drive coil area about 1.7 times smaller than that of a FARAD thruster [12]. The second value corresponds to a drive coil area about 11 times smaller than that of the TRW PIT drive coil, which is an annulus with an inner radius of ~ 20 cm, and an outer radius of ~ 50 cm [6, 7]. Therefore, the simulations presented here are for compact devices. It is important to note that R_{coil} is not the radius of the inlet, over which the propellant is uniformly distributed. The inlet radii corresponding to the smaller and larger values of R_{coil} are $R_{inlet} = 11$ cm and 27.5 cm, respectively. Simulations using TRW PIT size drive coils that cover the entire inlet area are currently being performed[2]. As expected, they show much stronger coupling between the power circuit and plasma, leading to higher I_{sp}. Fig. 3 shows the geometry and its mesh. The figure shows an $r - z$ plane cut through the cylindrically symmetric device. The z axis is the axis of the device. The disk shaped drive coil is at the left end of the device, normal to the page. The z axis passes through the center of the drive coil at $z = 0$. The current density at the drive coil is used as a boundary condition for the Faraday law equations for B_r and B_θ, allowing PCAPPS to advance the magnetic field in time. All other boundaries are treated as free stream boundaries.

3.2   Simulation Parameters

The values $L = 100$ nH, $C = 9\mu f$, $R = 6.7 \times 10^{-3}$ Ω, and $V_0 = 30$ kV are chosen for all simulations. These values are characteristic of TRW PIT experiments [7]. It is assumed the propellant fills the entire computational volume with an initial density $n_0 = 10^{21}$ m^{-3}. This value may be compared with the value $n_0 \sim 8.7 \times 10^{21}$ m^{-3} corresponding to actual TRW PIT experiments in which a 3 cm thick layer of 2 mg of Li propellant is distributed over a drive coil area ~ 0.66 m^2. The initial ionization level is assumed to be 5%. Simulations are performed using Li and Ar propellants, the difference between the two cases being the corresponding equations of state and mass densities. The assumption of propellant filling the entire computational volume is not realistic. Simulations using a more realistic initial

---

[2]The inlet is a remnant of the original LLFA geometry in PCAPPS. Current simulations, not described in this report, effectively replace the inlet by the drive coil, and extend the radius of the drive coil to the boundary of the computational domain.
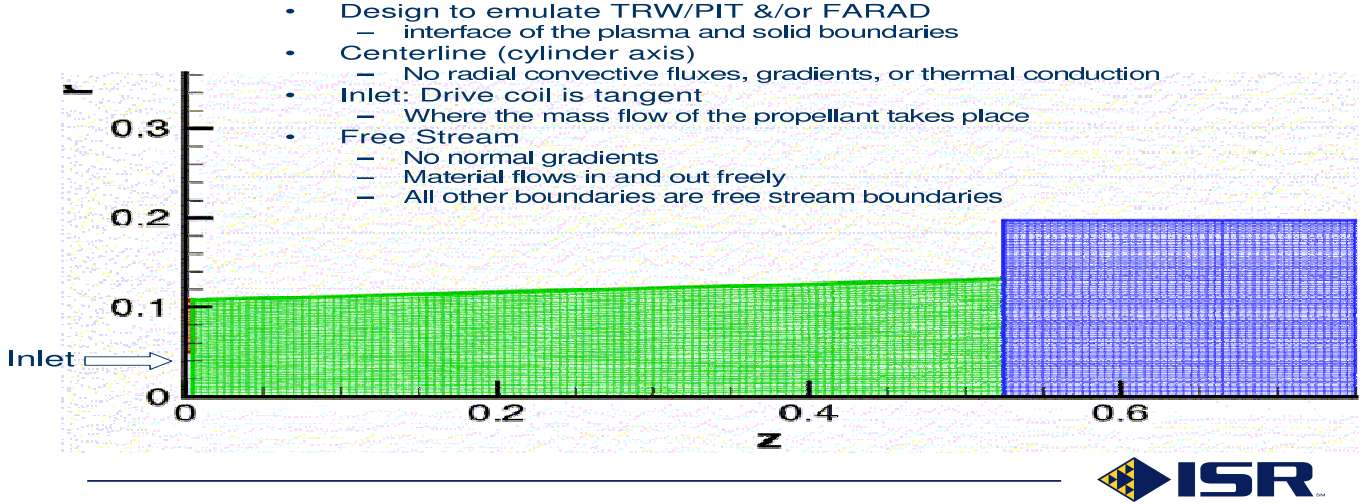
Figure 3: Device geometry. r and z are in meters.

density profile that decreases exponentially fast with increasing distance from the drive coil are currently being performed.

3.3 Simulation 1: $R_{coil} = 5.5$ cm, Uni-Directional Power Circuit-Plasma Coupling, Li Propellant

Uni-directional coupling means the power circuit acts on the plasma, but does not receive any feedback from the plasma. This coupling is defined by setting $V_{plasma} = 0$ in the power circuit equations. This simulation is performed to allow comparison of results for uni-directional and bi-directional coupling. As expected, there are major differences, emphasizing the importance of using a bi-directional power circuit-plasma coupling algorithm.

Figures 4 and 5 show the circuit current $I_{cir}(t)$ and plasma voltage $V_{plasma}(t)$ for a run lasting 50μ sec. I_{cir} shows oscillations with a period $\sim 5.9\mu$ sec, which is the natural frequency ω of the LRC circuit. For the chosen values of L, R, and C, $\omega \sim (LC)^{-1/2}$.

The magnitude of the current rises from zero to 2.65×10^5 A in the first quarter cycle as expected. It decreases by $\sim 18\%$ between successive peaks due to the circuit's resistance. B_r reaches a maximum value of 250 G at the drive coil. As shown by the next example in §3.4, this dissipation rate substantially increases when the power circuit-plasma coupling is bi-directional. V_{plasma} is periodic at approximately the same frequency as the power circuit. It rises to ~ 2200 V which is more than one order of magnitude below the initial capacitor voltage of 30 kV. This relatively small value of V_{plasma} is attributed to the relatively small power circuit-plasma coupling area of 9.5×10^{-3} m^2, which is the area of the drive coil, compared to a coupling area ~ 0.66 m^2 for the TRW PIT drive coil.

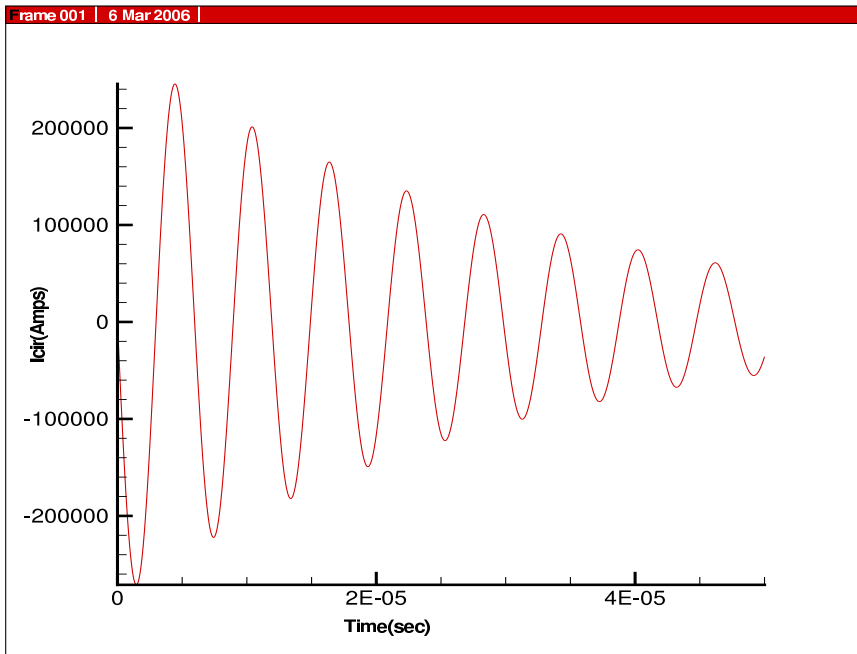Figures 6, 7, and 8 show the electron density at three successive times. The initial blue

10

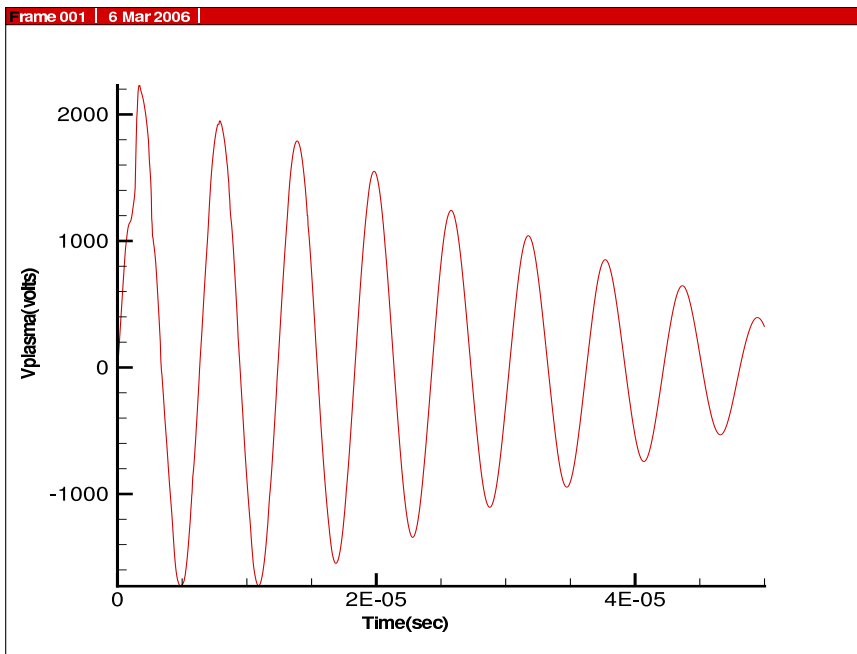Figure 4: Circuit current (A) vs. t(sec); R_{coil} = 5.5 cm, Uni-directional Coupling, Li Propellant.

Figure 5: V_{plasma} (V) vs. t (sec); R_{coil} = 5.5 cm, Uni-directional Coupling, Li Propellant.

background corresponds to the uniform initial background electron density of 5×10^{19} m^{-3}, which is the initial ionization fraction of 5 % times n_0. Figures 9, 10 and 11 show the
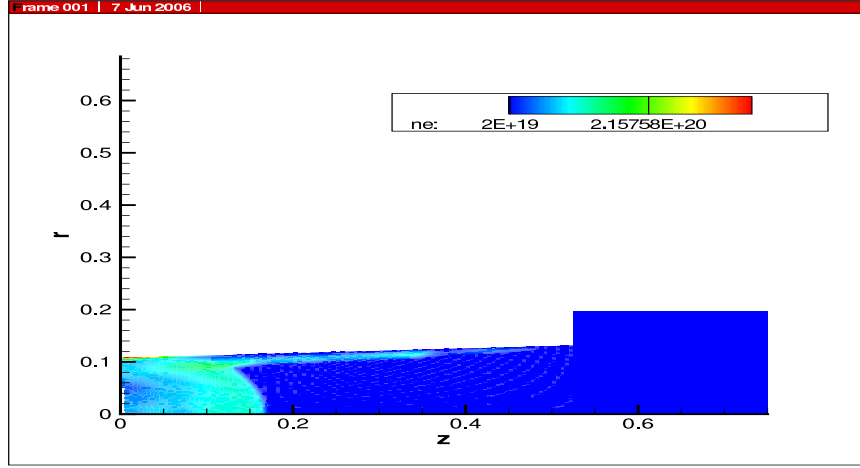

Figure 6: Electron number density (m^{-3}) at $t = 6.9\mu$ seconds; $R_{coil} = 5.5$ cm, Uni-directional Coupling, Li Propellant; r-z in meters.
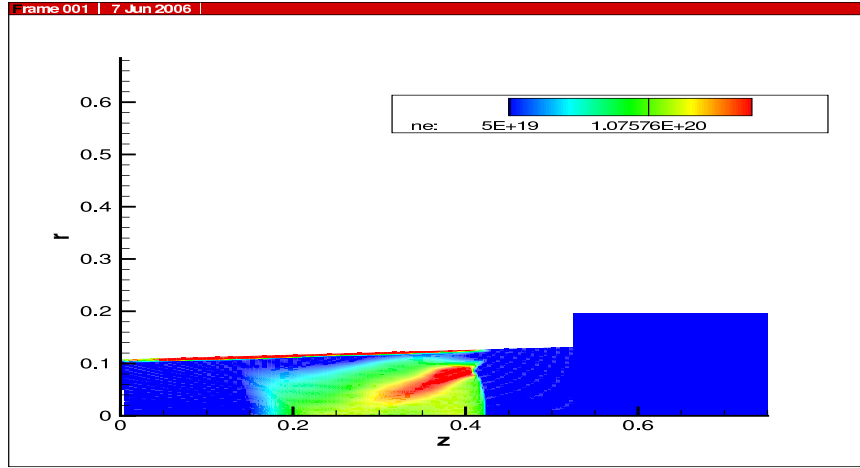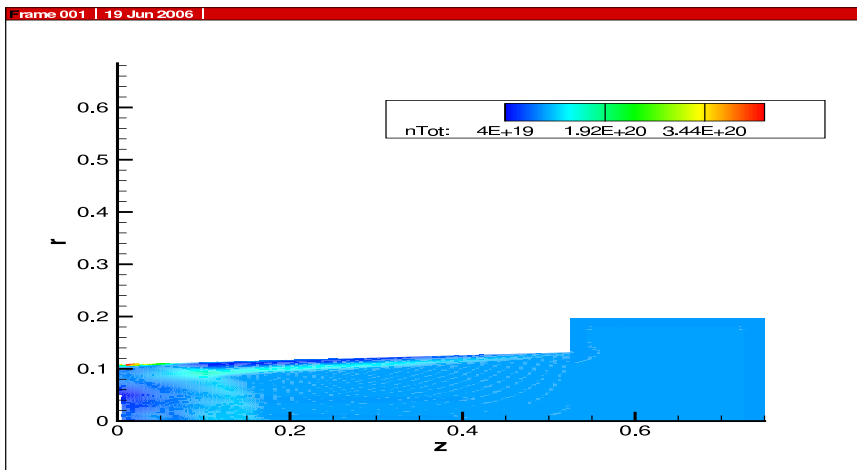

Figure 7: Electron number density (m^{-3}) at $t = 25\ \mu$ sec; $R_{coil} = 5.5$ cm, Uni-directional Coupling, Li Propellant; r-z in meters.

total number density at the same times. Figures 12, 13, and 14 show the corresponding axial velocities (here labeled V_z), and figures 15, 16, and 17 show the corresponding radial velocities (here labeled V_r). The large value of V_z near the inlet at later times is a result of the power circuit continuing to drive the plasma[3]. The profiles show plasma compression and acceleration from the drive coil to the exit on the far right. The maximum I_{sp} for this simulation is 3400 sec.

---

[3]Subsequent simulations show that using a sufficiently large drive coil radius causes almost all of the energy of the power circuit to be transferred to the plasma in approximately one oscillation of the circuit current.
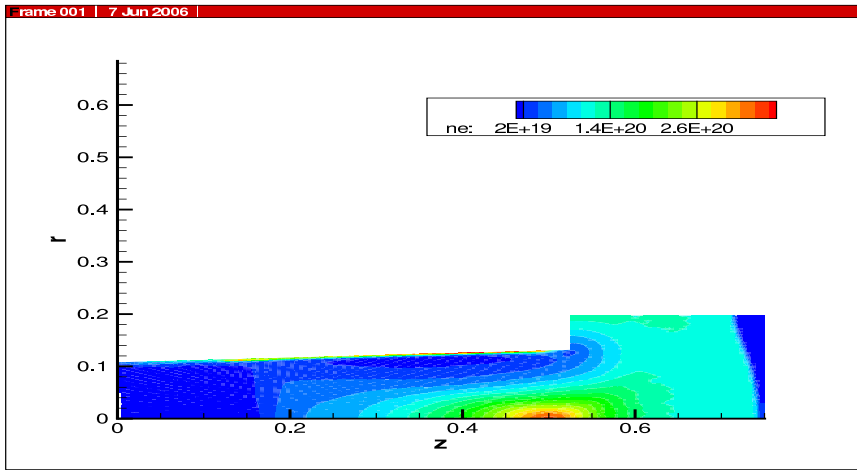
Figure 8: Electron number density (m^{-3}) at $t = 45\ \mu$ sec; $R_{coil} = 5.5$ cm, Uni-directional Coupling, Li Propellant; r-z in meters.

Figure 9: Total number density (m^{-3}) at $t = 6.9\ \mu$ seconds; $R_{coil} = 5.5$ cm, Uni-directional Coupling, Li Propellant; r-z in meters.
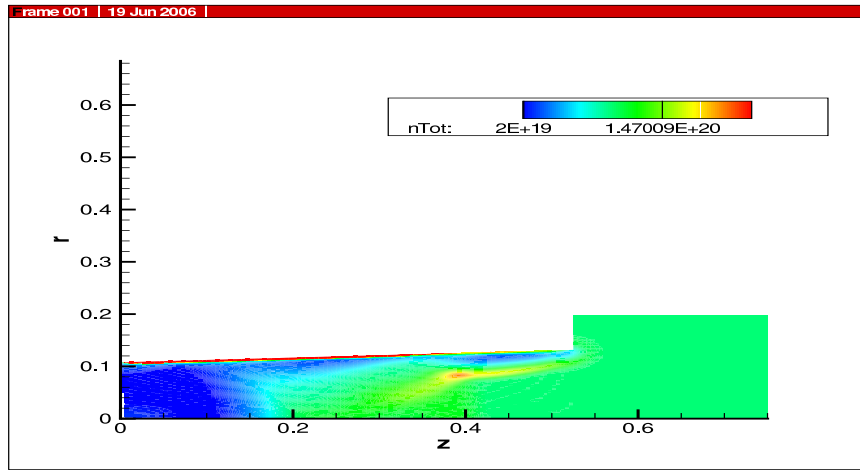
Figure 10: Total number density (m^{-3}) at $t = 25$ μ seconds; $R_{coil} = 5.5$ cm, Uni-directional Coupling, Li Propellant; r-z in meters.
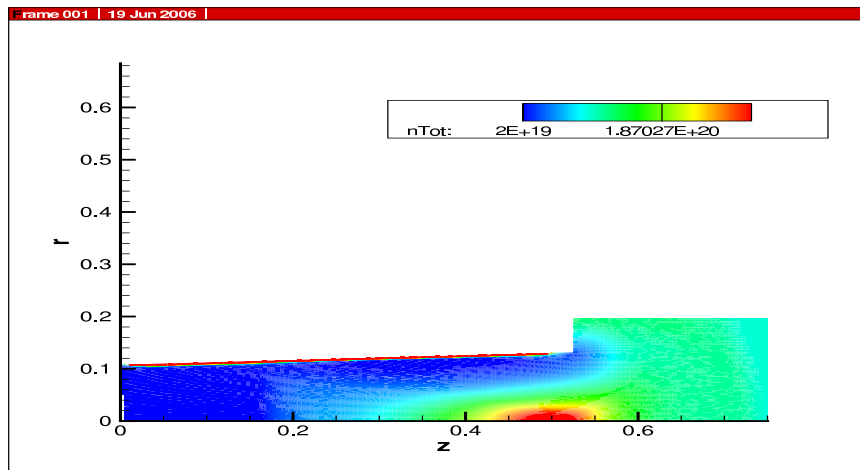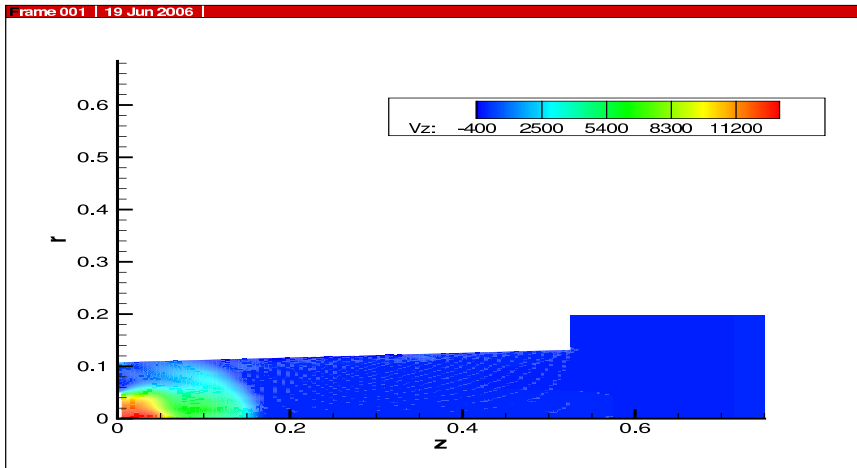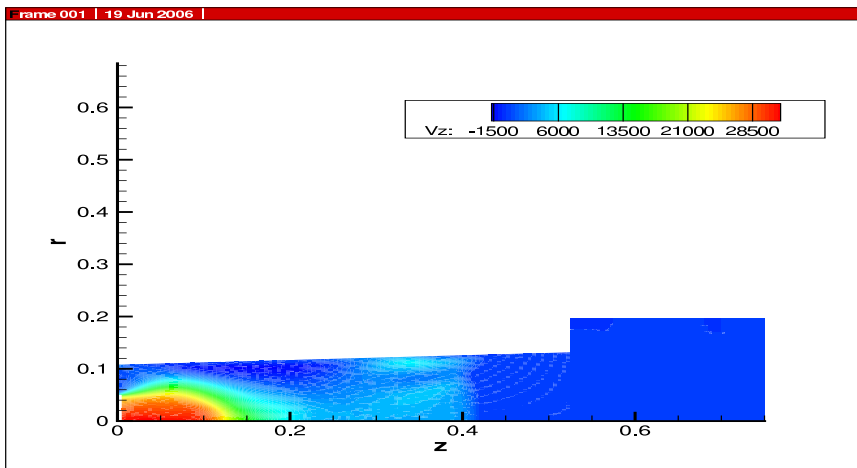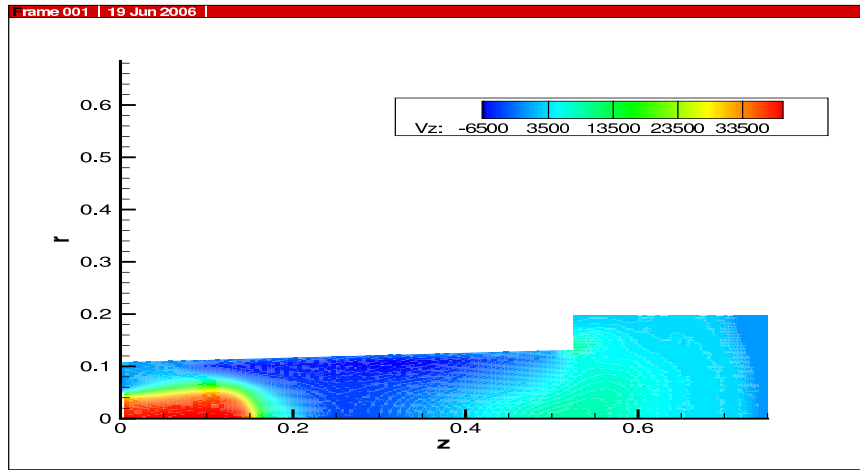

Figure 11: Total number density (m^{-3}) at $t = 45$ μ seconds; $R_{coil} = 5.5$ cm, Uni-directional Coupling, Li Propellant; r-z in meters.

14

Figure 12: Axial velocity $(m - sec^{-1})$ at $t = 6.9\,\mu$ seconds; $R_{coil} = 5.5$ cm, Uni-directional Coupling, Li Propellant; r-z in meters.
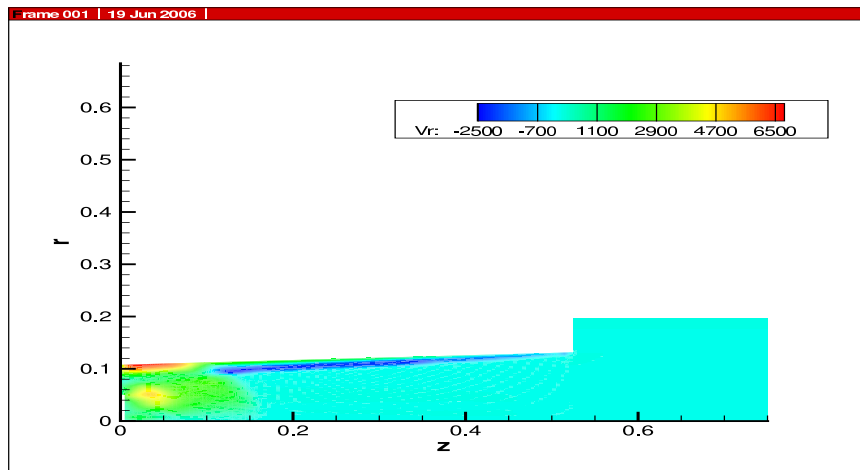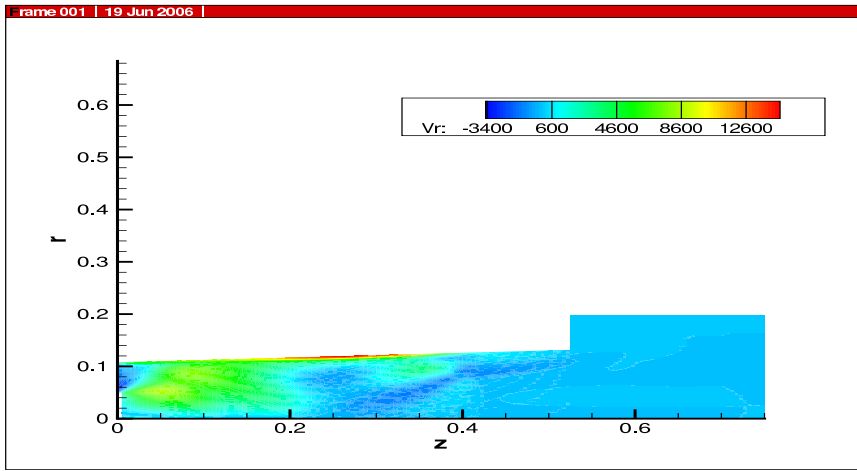

Figure 13: Axial velocity $(m - sec^{-1})$ at $t = 25\,\mu$ seconds; $R_{coil} = 5.5$ cm, Uni-directional Coupling, Li Propellant; r-z in meters.
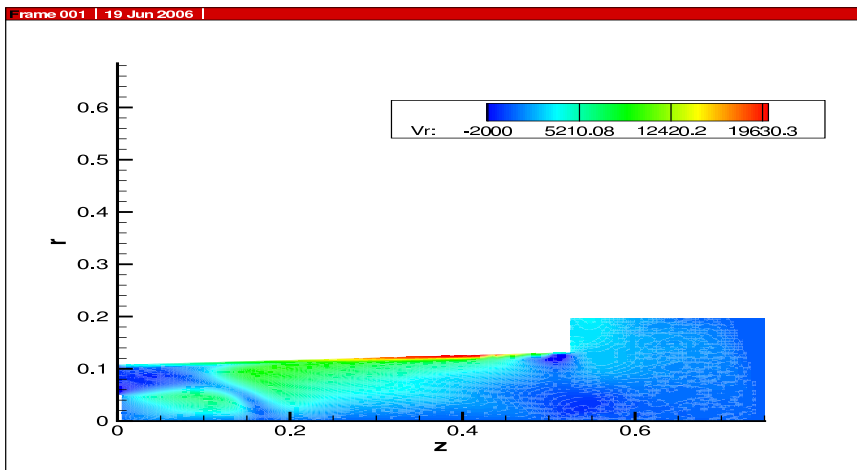
Figure 14: Axial velocity $(m - sec^{-1})$ at $t = 45$ μ seconds;$R_{coil} = 5.5$ cm, Uni-directional Coupling, Li Propellant; r-z in meters.

Figure 15: Radial velocity $(m - sec^{-1})$ at 6.9 μ seconds;$R_{coil} = 5.5$ cm, Uni-directional Coupling, Li Propellant; r-z in meters.

16

Figure 16: Radial velocity $(m - sec^{-1})$ at $t = 25$ μ seconds;$R_{coil} = 5.5$ cm, Uni-directional Coupling, Li Propellant; r-z in meters.

Figure 17: Radial velocity $(m - sec^{-1})$ at $t = 45$ μ seconds; $R_{coil} = 5.5$ cm, Uni-directional Coupling, Li Propellant; r-z in meters.

3.4 Simulation 2: $R_{coil} = 5.5$ cm, Bi-Directional Power Circuit-Plasma Coupling, Li Propellant

This simulation differs from Simulation 1 only in that there is now bi-directional coupling between the power circuit and the plasma. Figures 18 and 19 show $I_{cir}(t)$ and $V_{plasma}(t)$ for a period of 50 μ seconds. A comparison of Fig. 4 and Fig. 18 shows a significantly larger damping rate for the case of bi-directional coupling. The current in Fig. 4 decreases by $\sim 18\%$ per period. The current in Fig. 18 decreases by $30 - 40\%$ during each successive oscillation. The oscillation frequency for I_{cir} is essentially equal to the natural frequency ω of the power circuit. Since $\omega \sim (LC)^{-1/2}$ for the chosen values of L, R, and C, this implies that the inductive coupling between the power circuit and the plasma is not significant. In reality, this coupling can be significant. It is conjectured that the lack of inductive coupling in this simulation, and in the other simulations discussed below, is mainly due to two factors. The first is the unrealistic feature of the simulation that the propellant fills the entire computational volume, instead of the initial propellant distribution being a thin layer of gas on the drive coil. The second factor is that the mutual inductance between the plasma and the power circuit is expected to be proportional to the coupling area, which is the area of the drive coil. Then the coupling is $\propto R_d^2$. The maximum value of R_d used in the simulations is 13.75 cm. It may be that this value is not large enough to cause significant inductive coupling. Simulations are currently being performed to resolve this issue.
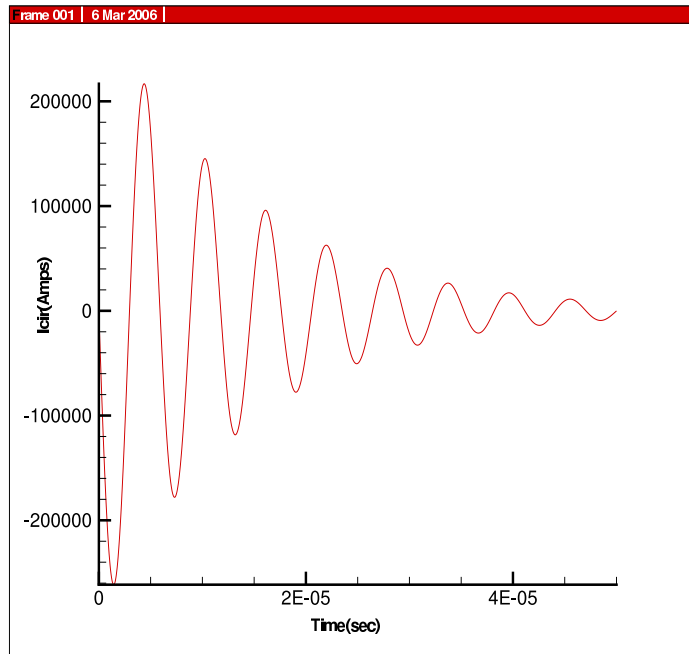

Figure 18: Power circuit current (A) vs. t (sec). $R_{coil} = 5.5$ cm, Bi-directional Coupling, Li Propellant.

Figures 20, 21, and 22 show the electron density at three successive times.

Figures 23, 24, and 25 show the total number density at the same times. Figures 26, 27, and 28 show the corresponding axial velocities, and figures 29, 30, and 31 show the corre-
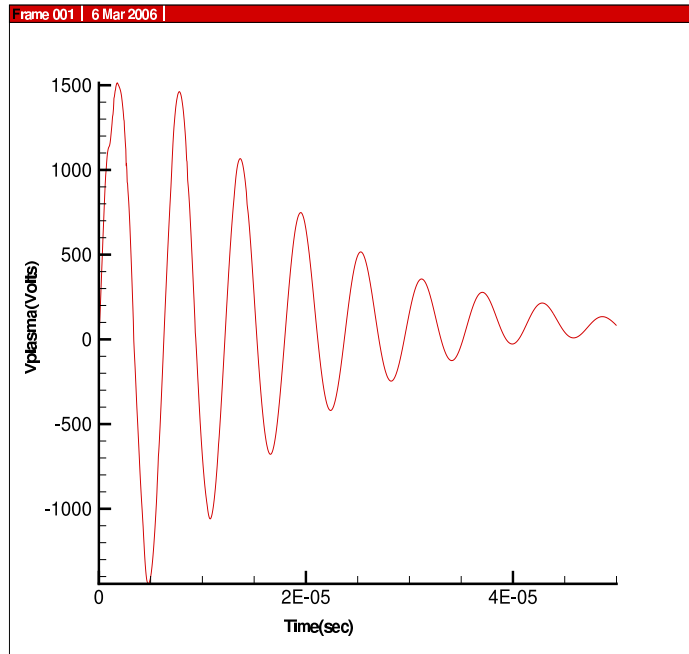
18

Figure 19: V_{plasma} (V) vs. t (sec). $R_{coil} = 5.5$ cm, Bi-directional Coupling, Li Propellant.
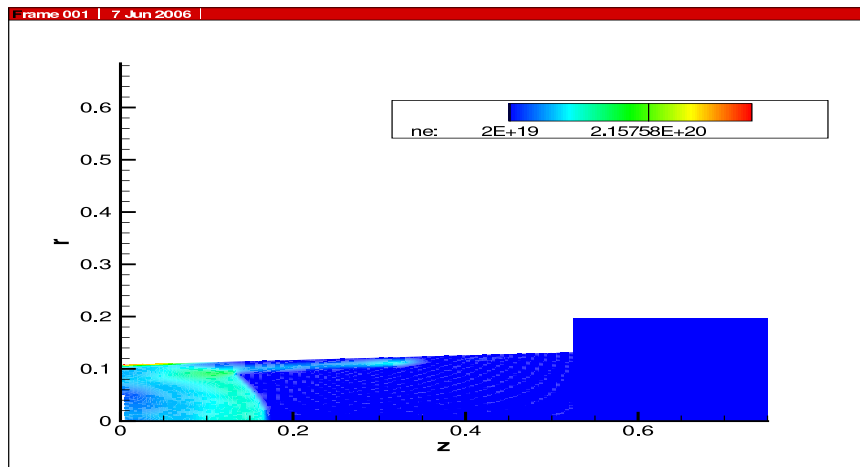

Figure 20: Electron number density (m^{-3}) at $t = 6.9\mu$ seconds. $R_{coil} = 5.5$ cm, Bi-directional Coupling, Li Propellant; r-z in meters.
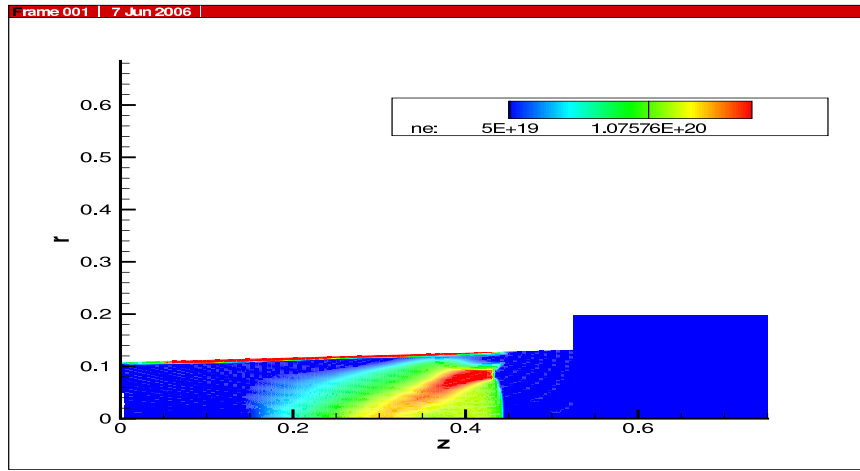
Figure 21: Electron number density (m^{-3}) at $t = 25 \, \mu$ seconds. $R_{coil} = 5.5$ cm, Bi-directional Coupling, Li Propellant; r-z in meters.
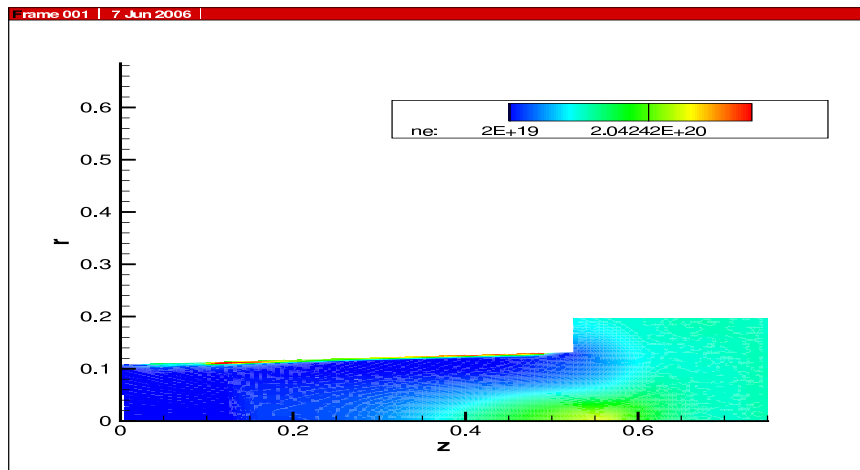

Figure 22: Electron number density (m^{-3}) at $t = 45 \, \mu$ seconds. $R_{coil} = 5.5$ cm, Bi-directional Coupling, Li Propellant; r-z in meters.

20

sponding radial velocities. The maximum I_{sp} achieved for this simulation is 2500 seconds. This value is significantly smaller than the corresponding value of 3400 seconds for Simulation 1. This reduction in the maximum value of I_{sp}, and the increase in the dissipation rate of the current in the power circuit over its value for Simulation 1 is believed to be due to the fact that, for bi-directional coupling, electrical energy in the plasma can be dissipated by the resistance of the power circuit, as well as by the plasma's own resistance. When the coupling is uni-directional, plasma electrical energy can only be dissipated by the plasma's resistance. Bi-directional coupling opens up a new channel for the resistive dissipation of plasma electrical energy, resulting in more energy being thermalized, and less being converted into bulk flow kinetic energy, leading to a lower I_{sp}.
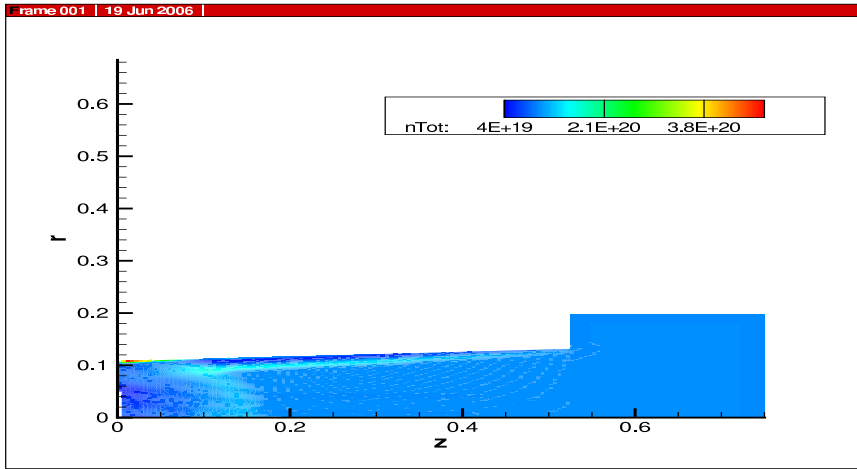

Figure 23: Total number density (m^{-3}) at $t = 6.9\,\mu$ seconds; $R_{coil} = 5.5$ cm, Bi-directional Coupling; r-z in meters.
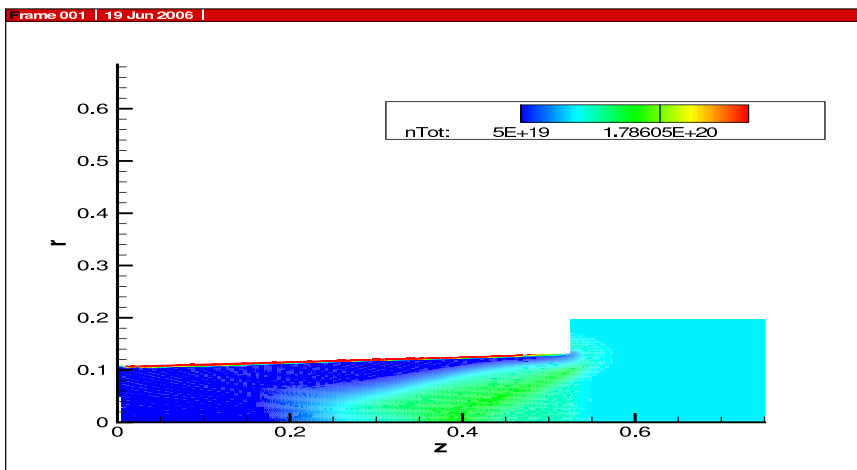

Figure 24: Total number density (m^{-3}) at $t = 25\,\mu$ seconds; $R_{coil} = 5.5$ cm, Bi-directional Coupling, Li Propellant; r-z in meters.
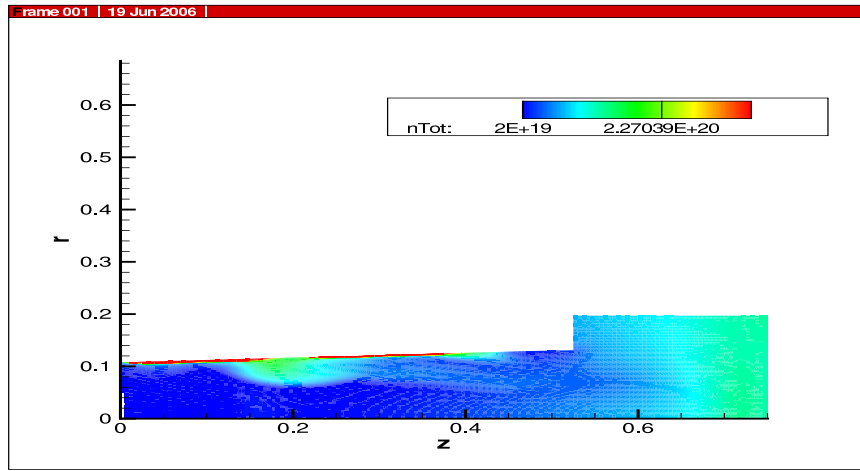
Figure 25: Total number density (m^{-3}) at $t = 45\,\mu$ seconds; $R_{coil} = 5.5$ cm, Bi-directional Coupling, Li Propellant; r-z in meters.
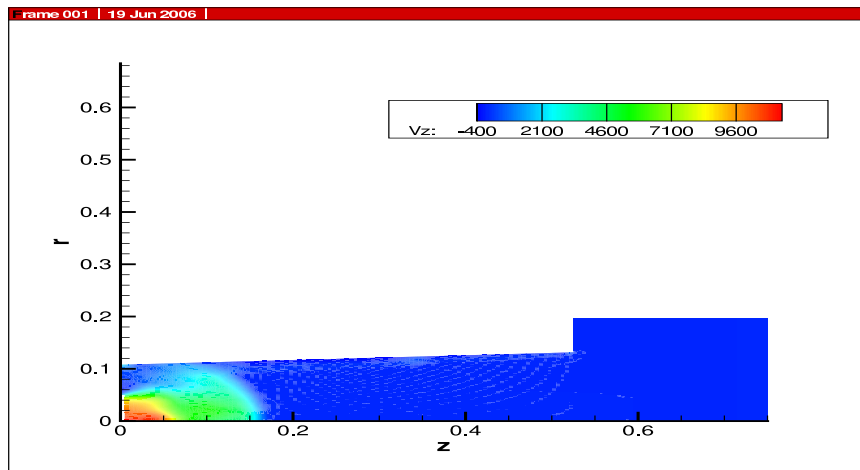

Figure 26: Axial velocity $(m - sec^{-1})$ at $t = 6.9\,\mu$ seconds; $R_{coil} = 5.5$ cm, Bi-directional Coupling, Li Propellant; r-z in meters.
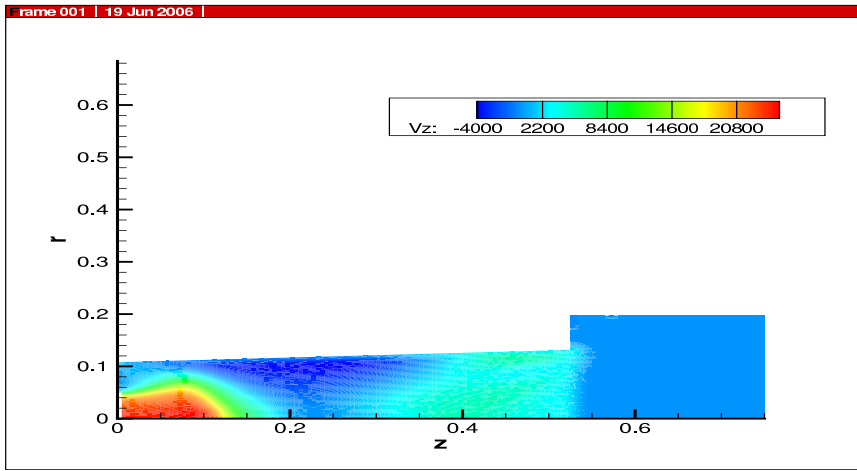
Figure 27: Axial velocity $(m - sec^{-1})$ at $t = 25$ μ seconds; $R_{coil} = 5.5$ cm, Bi-directional Coupling, Li Propellant; r-z in meters.
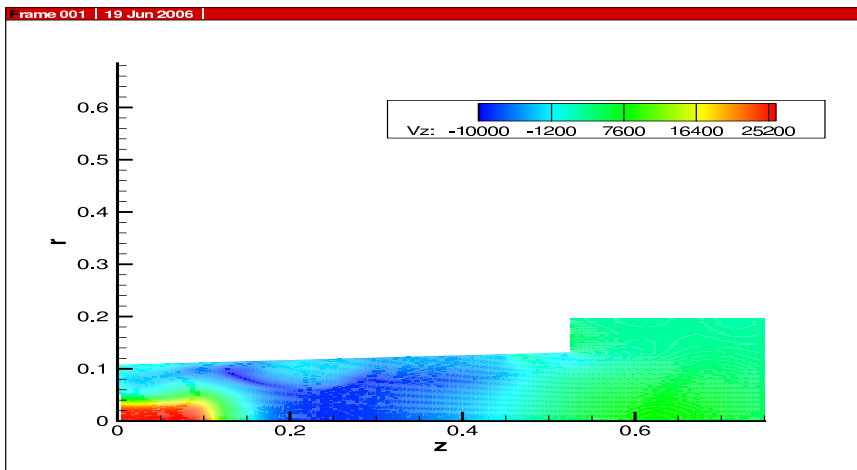

Figure 28: Axial velocity $(m - sec^{-1})$ at $t = 45$ μ seconds; $R_{coil} = 5.5$ cm, Bi-directional Coupling, Li Propellant; r-z in meters.
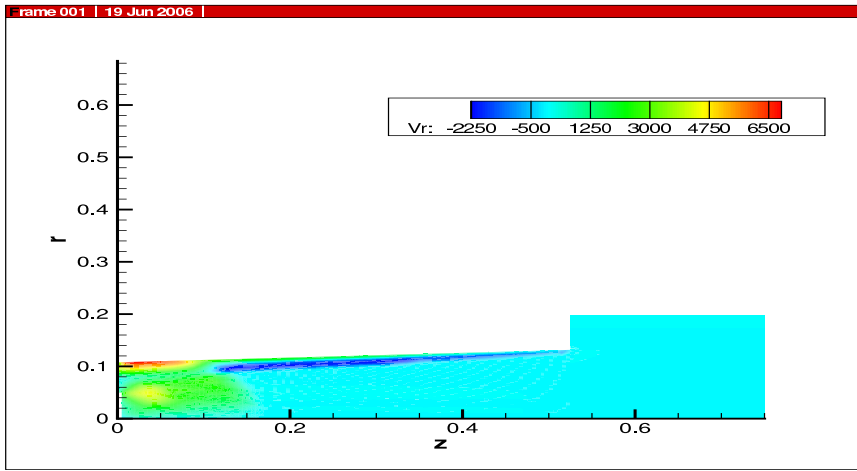
Figure 29: Radial velocity $(m - sec^{-1})$ at $t = 6.9\,\mu$ seconds; $R_{coil} = 5.5$ cm, Bi-directional Coupling, Li Propellant; r-z in meters.
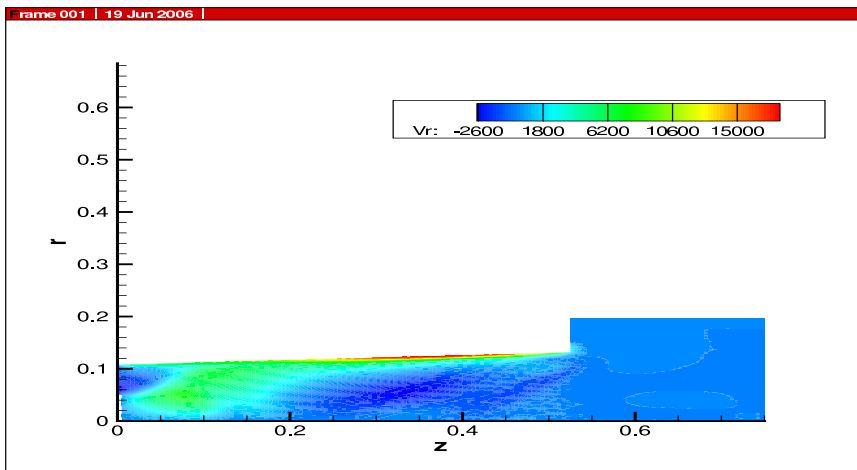

Figure 30: Radial velocity $(m - sec^{-1})$ at $t = 25\,\mu$ seconds; $R_{coil} = 5.5$ cm, Bi-directional Coupling, Li Propellant; r-z in meters.
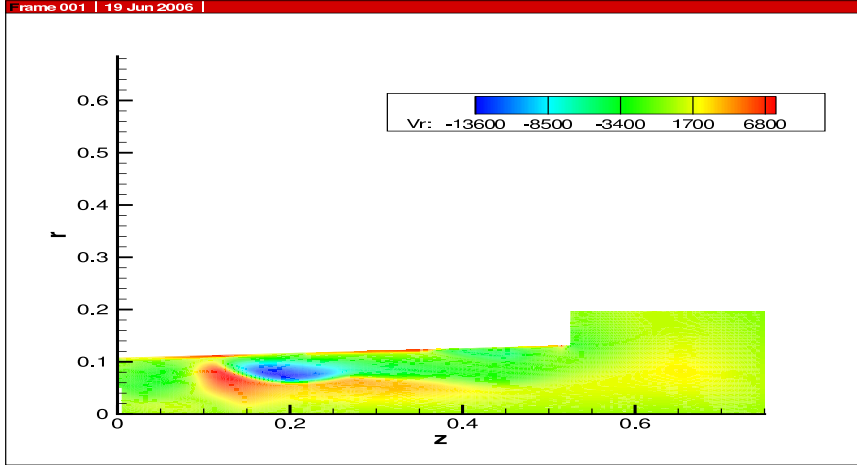
Figure 31: Radial velocity $(m - sec^{-1})$ at $t = 45$ μ seconds; $R_{coil} = 5.5$ cm, Bi-directional Coupling, Li Propellant; r-z in meters.

3.5 Simulation 3: $R_{coil} = 13.75$ cm, Bi-Directional Power Circuit-Plasma Coupling, Li Propellant

Here the drive coil-plasma coupling area is increased by a factor of 6.25 over that for Simulation 2. $I_{cir}(t)$ and $V_{plasma}(t)$ are shown in figures 32 and 33. A comparison of figure 32 with figure 18 shows that the current damps at about the same rate as for Simulation 2. This is believed to be mainly due to the result of the unrealistic assumption of a constant drive coil resistance R. Since the area of the drive coil is increased by the factor 6.25 over that in Simulation 2, the resistance should increase by approximately the same factor. This is expected to increase the current damping rate by about the same factor. A comparison of figure 33 with figure 19 shows that V_{plasma} decreases more rapidly than for Simulation 2. This is believed to be due to the larger coupling area allowing for more rapid dissipation of plasma electrical energy by the power circuit resistance.

Figures 34, 35, and 36 show the total density at three successive times.
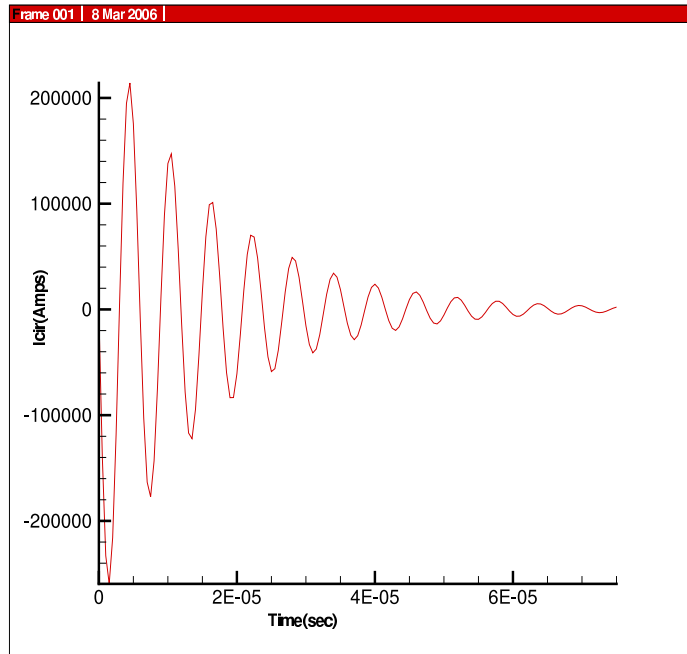
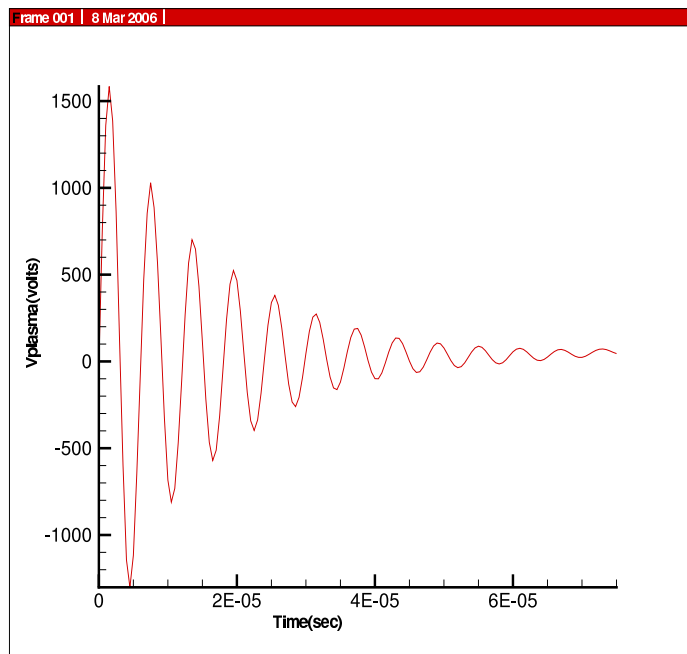Figure 32: Circuit current (A) vs. t (sec). $R_{coil} = 13.75$ cm, Bi-directional Coupling, Li Propellant.

Figure 33: Plasma voltage (V) vs. t (sec). $R_{coil} = 13.75$ cm, Bi-directional Coupling, Li Propellant.
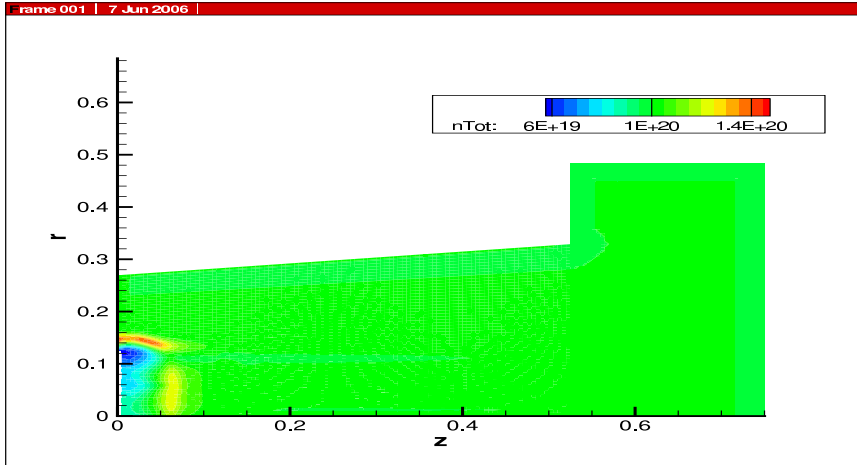
26

Figure 34: Total number density (m^{-3}) at $t = 10\,\mu$ seconds. $R_{coil} = 13.75$ cm, Bi-directional Coupling, Li Propellant; r-z in meters.
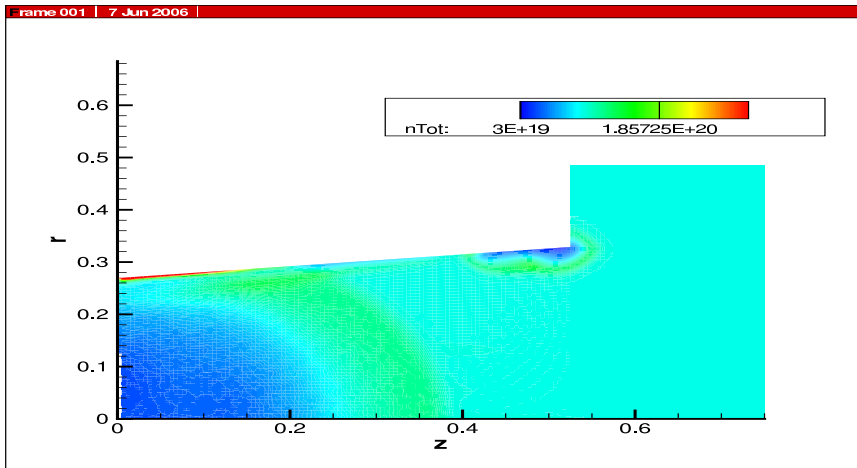

Figure 35: Total number density (m^{-3}) at $t = 25\,\mu$ seconds. $R_{coil} = 13.75$ cm, Bi-directional Coupling, Li Propellant; r-z in meters.

Figures 37, 38, and 39 show the electron density at the same times.

Figures 40, 41, and 42 show the corresponding axial velocity.

Figures 43, 44, and 45 show the corresponding radial velocity. The duration of this simulation is 75 μ seconds. The increase in runtime over that of Simulation 2 is necessary to fully resolve the plasma dynamics since the axial velocity is much smaller than for Simulation 2. This decrease in axial flow velocity is believed to be due to the greater dissipation rate of plasma electrical energy by the resistance R of the power circuit, thereby decreasing the energy available for propellant acceleration. This is a consequence of the bi-directional coupling of the power circuit and plasma allowing plasma electrical energy to be dissipated by the circuit resistance as well as by the plasma resistance. The maximum value of I_{sp} for this simulation is 620 seconds.
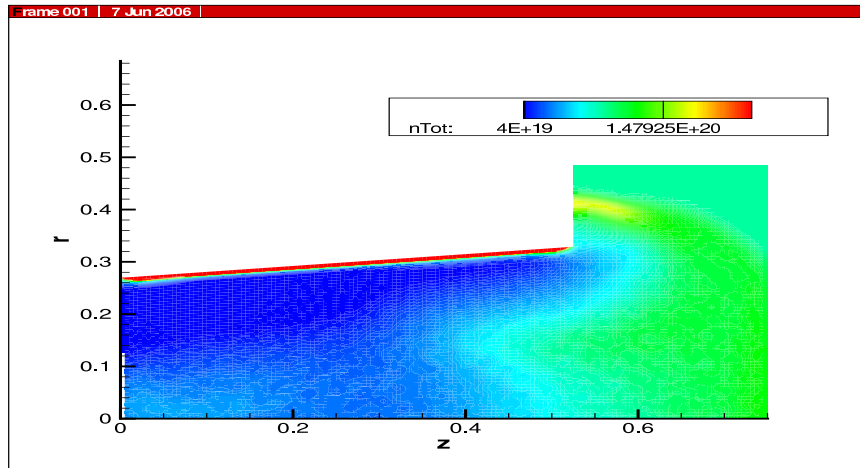
Figure 36: Total number density (m^{-3}) at $t = 45\ \mu$ seconds. $R_{coil} = 13.75$ cm, Bi-directional Coupling, Li Propellant; r-z in meters.
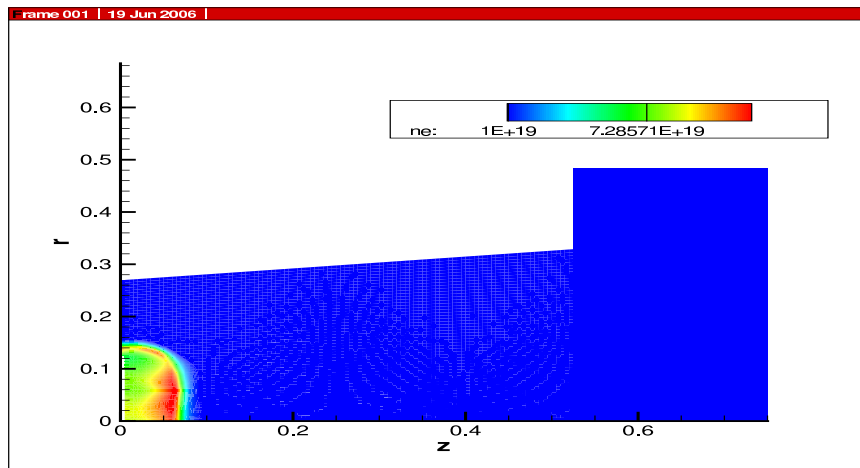

Figure 37: Electron number density (m^{-3}) at $t = 10\ \mu$ seconds. $R_{coil} = 13.75$ cm, Bi-directional Coupling, Li Propellant; r-z in meters.

28

Figure 38: Electron number density (m^{-3}) at $t = 25\ \mu$ seconds. $R_{coil} = 13.75$cm, Bi-directional Coupling, Li Propellant; r-z in meters.

Figure 39: Electron number density (m^{-3}) at $t = 45\ \mu$ seconds. $R_{coil} = 13.75$cm, Bi-directional Coupling, Li Propellant; r-z in meters.
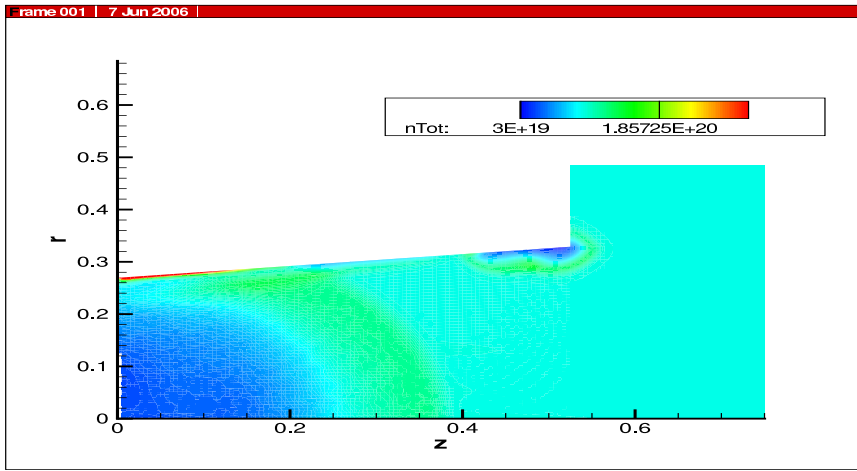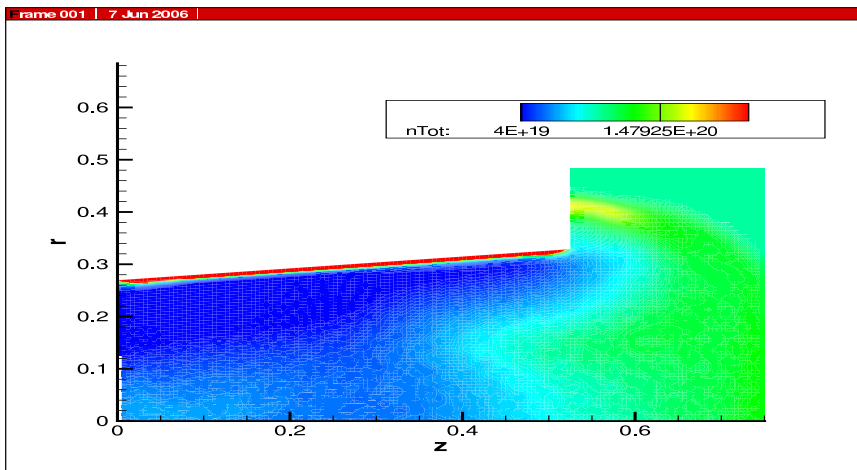
Figure 40: Axial velocity $(m - sec^{-1})$ at $t = 10\,\mu$ seconds. $R_{coil} = 13.75$ cm, Bi-directional Coupling, Li Propellant; r-z in meters.

Figure 41: Axial velocity $(m - sec^{-1})$ at $t = 25\,\mu$ seconds. $R_{coil} = 13.75$ cm, Bi-directional Coupling, Li Propellant; r-z in meters.

Figure 42: Axial velocity $(m-sec^{-1})$ at $t = 45\,\mu$ seconds. $R_{coil} = 13.75$ cm, Bi-directional Coupling, Li Propellant; r-z in meters.
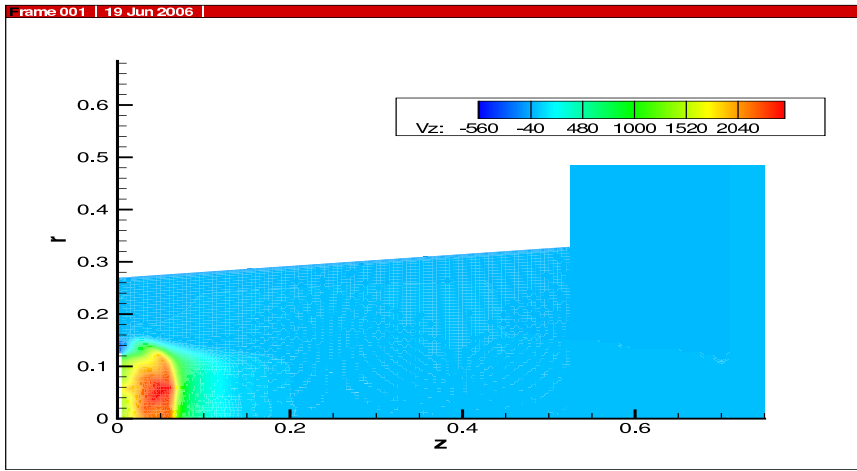

Figure 43: Radial velocity $(m-sec^{-1})$ at $t = 10\,\mu$ seconds. $R_{coil} = 13.75$ cm, Bi-directional Coupling, Li Propellant; r-z in meters.
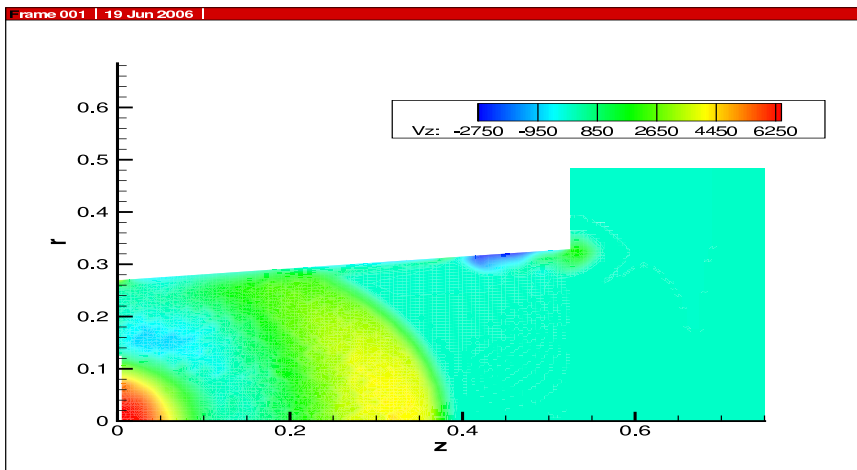
Figure 44: Radial velocity $(m - sec^{-1})$ at $t = 25$ μ seconds. $R_{coil} = 13.75$ cm, Bi-directional Coupling, Li Propellant; r-z in meters.
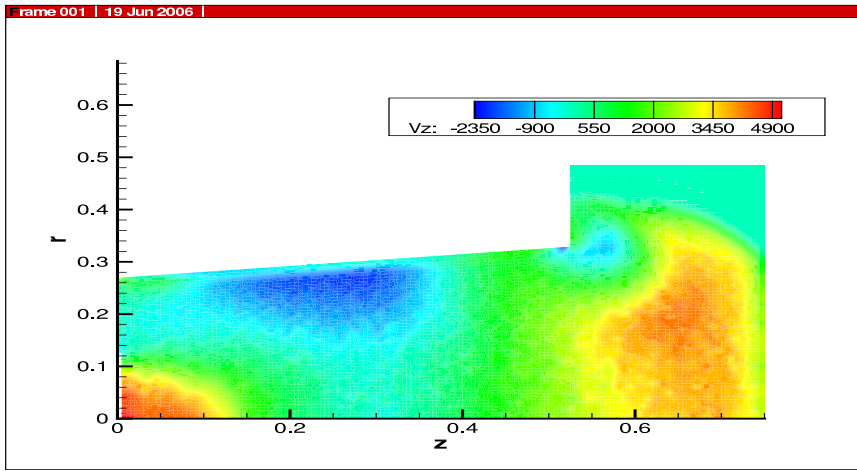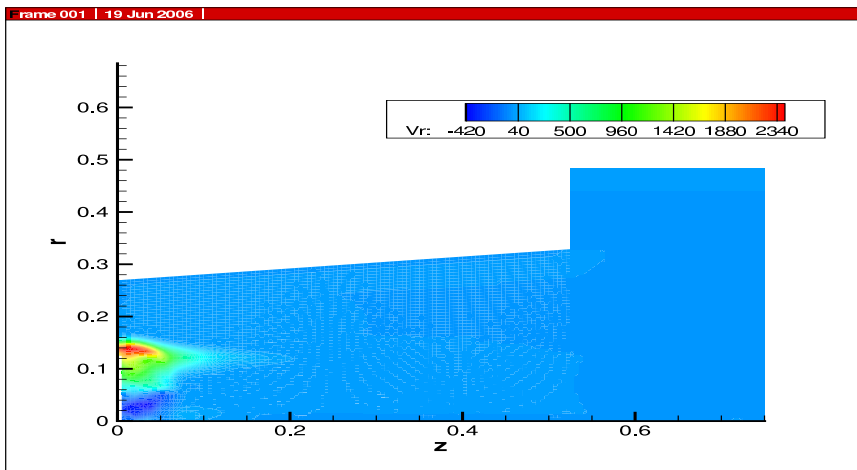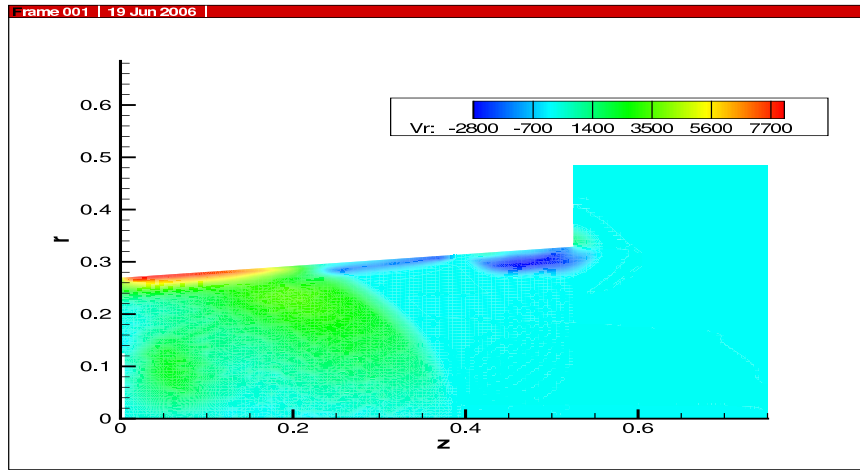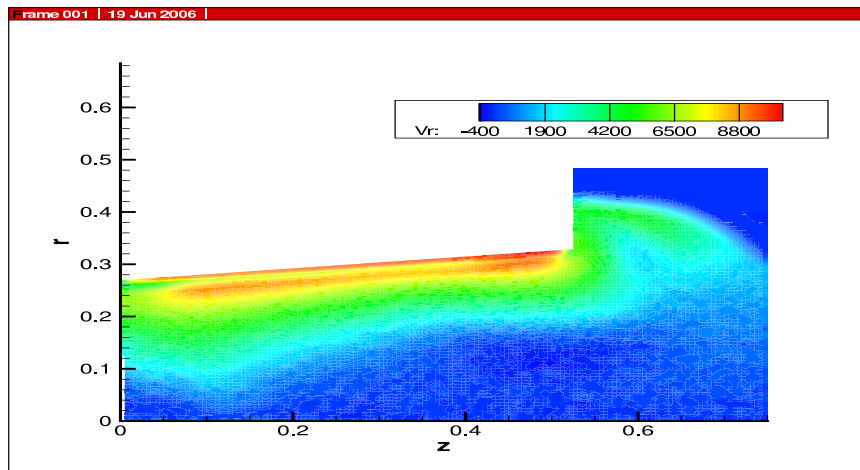

Figure 45: Radial velocity $(m - sec^{-1})$ at $t = 45$ μ seconds. $R_{coil} = 13.75$ cm, Bi-directional Coupling, Li Propellant; r-z in meters.

32

3.6 Simulation 4: $R_{coil} = 13.75$ cm, Bi-Directional Power Circuit-Plasma Coupling, Ar Propellant

This simulation is identical to Simulation 3 except that Ar is used as a propellant instead of Li. The masses of Ar and Li are 39.948 amu and 6.94 amu. The difference between the Li and Ar cases enters the model through the mass density, and equation of state.

Figures 46 and 47 show $I_{cir}(t)$ and $V_{plasma}(t)$. Comparison of these figures with figures 32 and 33 for Simulation 3 show that all profiles oscillate with a period essentially equal to the natural frequency $\omega \sim 5.9\mu$ sec of the power circuit, but that the amplitude of I_{cir} is significantly larger for the case of Ar. As for Simulation 2, the fact that the oscillation frequency is ω, which is $\sim (LC)^{-1/2}$, indicates there is no significant inductive coupling between the plasma and the power circuit for these simulations. The result that the damping rate for I_{cir} is smaller in the case of Ar than in the case of Li is due to the fact that relatively little work is done by the Lorentz force on the plasma during the simulation with Ar compared with that done during the simulation with Li. For a given axial Lorentz force F_z, the acceleration of Ar is less than that of Li by roughly the mass ratio. The power applied by the power circuit to accelerate the plasma is $\sim F_z V_z$, which is smaller for Ar than for Li due to the smaller value of V_z.

For given F_z, the ratio of the maximum values of I_{sp} for the Li and Ar cases should be approximately equal to the inverse ratio of their masses. The maximum value of I_{sp} for this simulation, obtained from figure 50, is 140 seconds. Then these ratios are 4.43 and 5.64.

As a result of the increase in mass of the propellant, the plasma only moves a distance ~ 0.2 m during the 75 μ sec duration of the simulation.
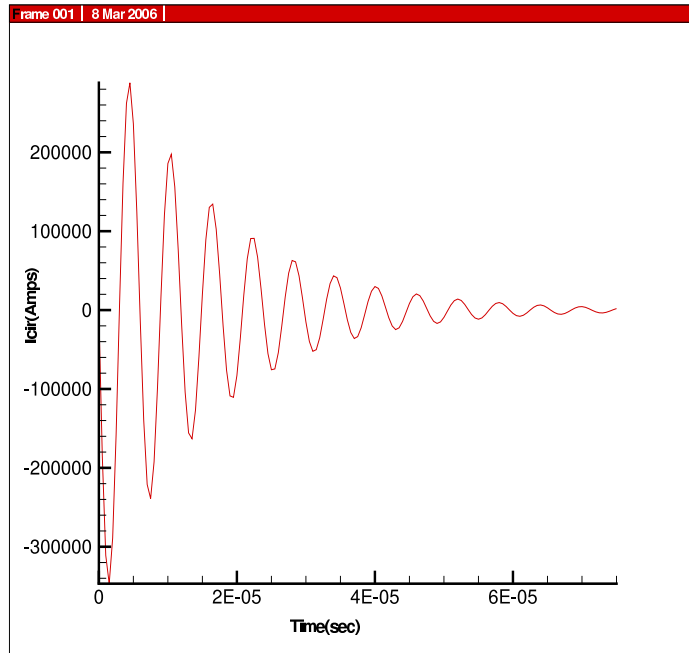

Figure 46: Circuit current (A) vs. t (sec). $R_{coil} = 13.75$ cm, Bi-directional Coupling, Ar Propellant
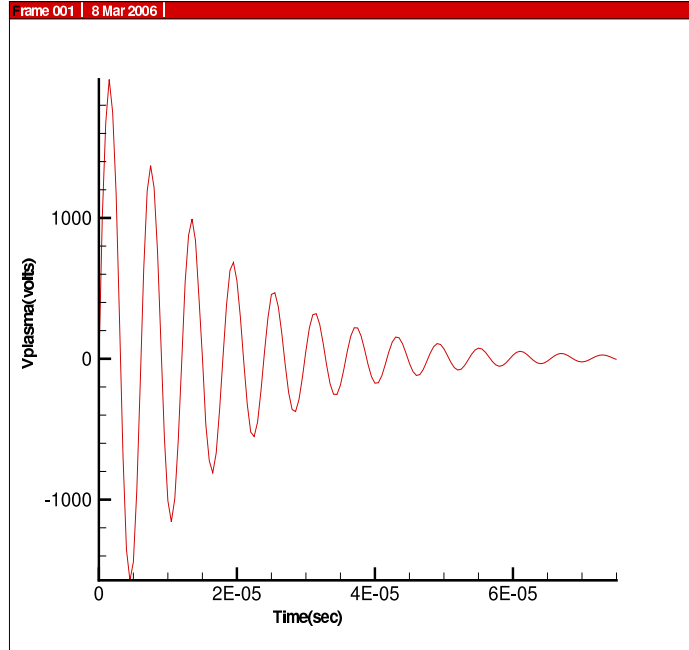
Figure 47: Plasma voltage (V) vs. t (sec). $R_{coil} = 13.75$ cm, Bi-directional Coupling, Ar Propellant.

Figures 48, 49, 50, and 51 show the total number density, electron number density, and axial and radial velocities at $t = 75$ μ sec. Increasing the initial capacitor voltage V_0 increases the acceleration. However, ongoing work shows that using a realistic initial density profile, a significantly higher I_{sp} is obtained for Ar without changing V_0.

34

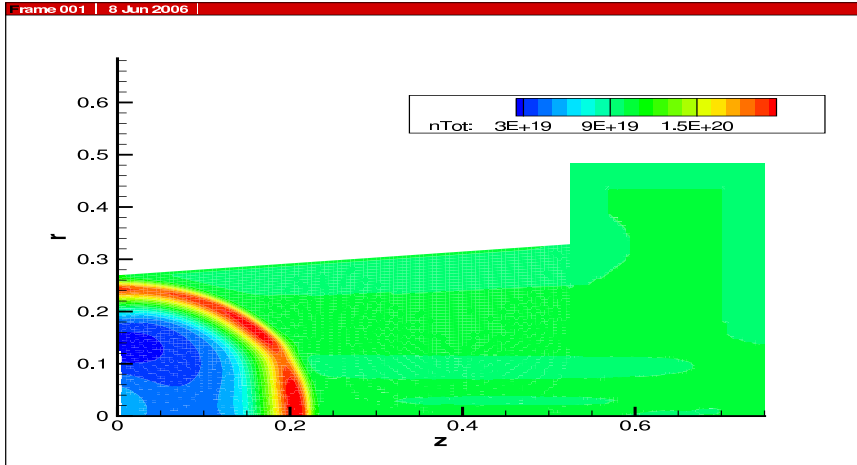Figure 48: Total number density (m^{-3}) at $t = 75\ \mu$ seconds. $R_{coil} = 13.75$ cm, Bi-directional Coupling, Ar Propellant; r-z in meters.
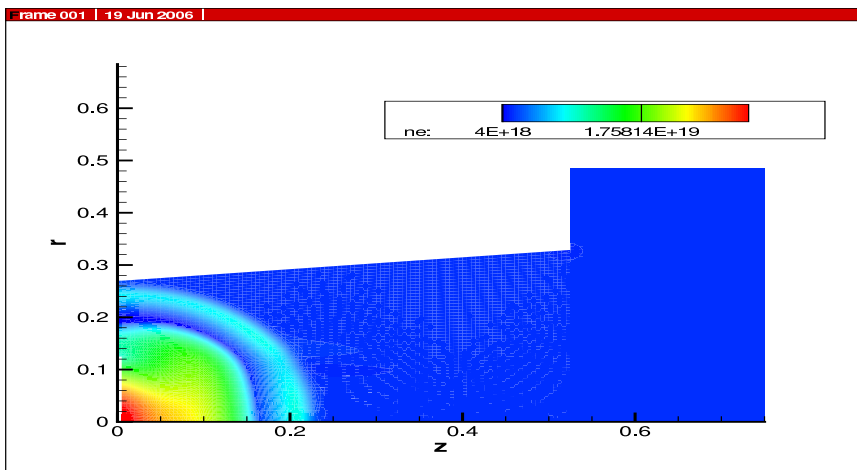

Figure 49: Electron number density (m^{-3}) at $t = 75\ \mu$ seconds. $R_{coil} = 13.75$ cm, Bi-directional Coupling, Ar Propellant; r-z in meters.

4.0 Summary

PCAPPS was modified to model pulsed inductive thrusters by: (1) Changing the geometry of the computational domain from that corresponding to an LLFA to that corresponding to a PPA; (2) Adding the radial component of the magnetic field to the model; (3) Implementing a general, first principles based power circuit-plasma coupling algorithm. These modifications are the first in a series of modifications to generalize PCAPPS to a complete 2.5 D simulation tool for cylindrically symmetric PPA's, and similar pulsed power devices.

An accurate algorithm for modeling power circuit-plasma coupling in PPA simulations is necessary for the simulation to be useful for designing, optimizing, and predicting the op-
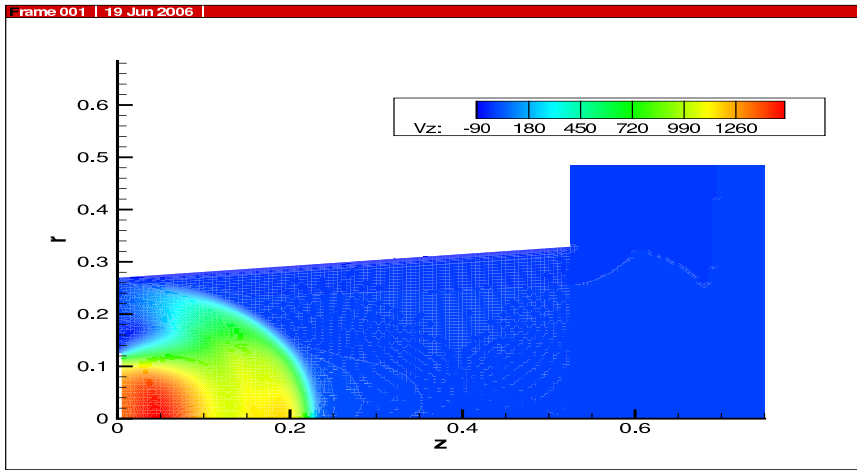
Figure 50: Axial velocity $(m - sec^{-1})$ at $t = 75$ μ seconds. $R_{coil} = 13.75$ cm, Bi-directional Coupling, Ar Propellant; r-z in meters.
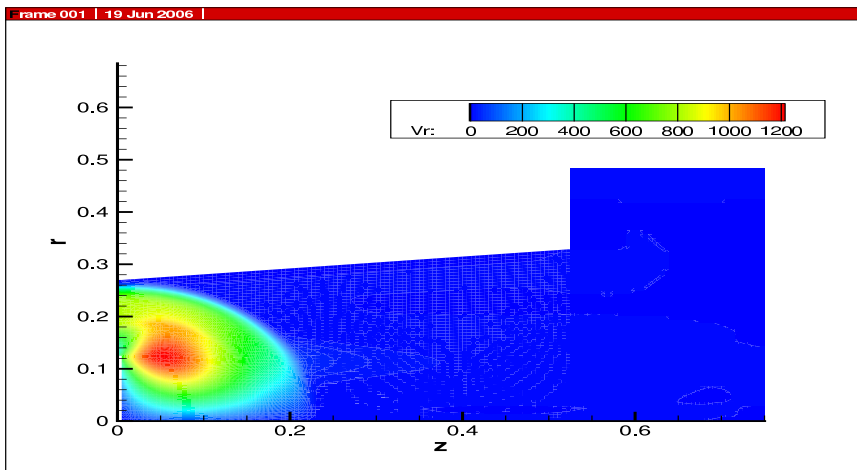

Figure 51: Radial velocity $(m - sec^{-1})$ at $t = 75$ μ seconds. $R_{coil} = 13.75$ cm, Bi-directional Coupling, Ar Propellant; r-z in meters.

36

eration of PPA's. Previous power circuit-plasma coupling algorithms are uni-directional or represent the plasma as a circuit coupled to the power circuit through a mutual inductance. For the PPA project, ISR conceived and implemented a self consistent, general, first principles based power circuit-plasma coupling algorithm. This algorithm appears to be new. The implementation was done using an L, R, C power circuit, and the Ohm's law in the original version of PCAPPS. However, the algorithm is easily implemented for an arbitrary power circuit and Ohm's law. For a power circuit that is not easily represented as a set of differential equations that may be solved analytically or numerically, a general circuit modeling tool such as PSPICE may be used to solve for the drive coil current that provides the required boundary condition for PCAPPS. PCAPPS then provides an updated voltage across the drive coil due to the plasma electric field. This voltage drop is represented as an EMF in series with the drive coil resistance and inductance in the power circuit, allowing PSPICE to compute an updated drive coil current. Changing the Ohm's law in PCAPPS simply changes the algebraic equation for the plasma electric field.

Since the end of the PPA project reported on here, PCAPPS was further modified in two important ways. The first was to expand the drive coil area to cover the entire area of the computational boundary at the back wall $z = 0$. This provides a more accurate representation of the geometry of real PPA's The second modification was to implement a realistic initial propellant density profile, modeled as a density distribution that falls off exponentially with increasing distance from the drive coil. Simulation results incorporating these modifications will be reported during the current phase of the project in 2006 - 2007.

References

[1] Sankaran, K., *MS thesis*, Princeton University Department of Mechanical and Aerospace Engineering, Jan 2001.

[2] Sankaran, K., *Ph.D. thesis*, Princeton University Department of Mechanical and Aerospace Engineering, Jan 2005.

[3] Choueiri, E. Y., *MS thesis*, A Scaling Strategy for the Preliminary Design of MPD Thrusters, 1983.

[4] Choueiri, E. Y., *Phys. of Plasmas*, 6(5):2290, 1999.

[5] Post, D.E., R.V. Jensen, C.B. Tarter, W.H. Grasberger, and W.A. Lokke., *Princeton Plasma Physics Laboratory 1352*, 1972.

[6] Loveberg, R.H., and C.L. Dailey, *A PIT Primer*, 1993.

[7] Dailey, C.L., *Technical Report AFRL-TR-71-107*, 1971.

[8] Mikellides, P.G., and C. Neilly, *AIAA 2004-4092*, 2004.

[9] Godlewski, E. and P.A. Raviart, *Numerical Approximation of Hyperbolic Systems of Conservation Laws*, Springer, 1996.

[10] Roe, *J. Comput. Phys.*, 43:357, 1981.

[11] Polk, J.E., *Personal Communications.*, NASA-JPL, 2003.

[12] Choueiri, E.Y., and K.A. Polzin, *AIAA-2004-3940*, 2004.

REPORT DOCUMENTATION PAGE

1. REPORT DATE (DD-MM-YYYY)	2. REPORT TYPE	3. DATES COVERED (From - To)
01-01-2009	Contractor Report	09/2004 – 03/2006

4. TITLE AND SUBTITLE	5a. CONTRACT NUMBER
Pulsed Plasma Accelerator Modeling	5b. GRANT NUMBER NNM04AA67G
	5c. PROGRAM ELEMENT NUMBER
6. AUTHOR(S) M. Goodman, F. Kazeminezhad, and T. Owens	5d. PROJECT NUMBER
	5e. TASK NUMBER
	5f. WORK UNIT NUMBER

7. PERFORMING ORGANIZATION NAME(S) AND ADDRESS(ES)	8. PERFORMING ORGANIZATION REPORT NUMBER
The Institute for Scientific Research, Inc. 320 Adams Street, P.O. Box 2720, Fairmont, WV 26555-2720	M–1249

9. SPONSORING/MONITORING AGENCY NAME(S) AND ADDRESS(ES)	10. SPONSORING/MONITOR'S ACRONYM(S)
J. Bonometti, Emerging Propulsion Technologies Manager In-Space Propulsion George C. Marshall Space Flight Center Marshall Space Flight Center, Alabama 35812	NASA
	11. SPONSORING/MONITORING REPORT NUMBER NASA/CR—2009–215635

12. DISTRIBUTION/AVAILABILITY STATEMENT
Unclassified-Unlimited
Subject Category 20
Availability: NASA CASI 443–757–5802

13. SUPPLEMENTARY NOTES
Prepared for the Space Systems Department, Engineering Directorate
Technical Monitor: J. Bonometti

14. ABSTRACT

This report presents the main results of the modeling task of the PPA project. The objective of this task is to make major progress towards developing a new computational tool with new capabilities for simulating cylindrically symmetric 2.5 dimensional (2.5 D) PPA's. This tool may be used for designing, optimizing, and understanding the operation of PPA's and other pulsed power devices. The foundation for this task is the 2-D, cylindrically symmetric, magnetohydrodynamic (MHD) code PCAPPS (Princeton Code for Advanced Plasma Propulsion Simulation). PCAPPS was originally developed by Sankaran (2001, 2005) to model Lithium Lorentz Force Accelerators (LLFA's), which are eletrode based devices, and are typically operated in continuous magnetic field to the model, and implementing a first principles, self-consistent algorithm to couple the plasma and power circuit that drives the plasma dynamics.

15. SUBJECT TERMS
electric propulsion, pulsed plasma accelerator, pulsed inductive thruster, pulsed power, plasma modeling

16. SECURITY CLASSIFICATION OF:			17. LIMITATION OF ABSTRACT	18. NUMBER OF PAGES	19a. NAME OF RESPONSIBLE PERSON STI Help Desk at email: help@sti.nasa.gov
a. REPORT	b. ABSTRACT	c. THIS PAGE	UU	52	
U	U	U			19b. TELEPHONE NUMBER (Include area code) STI Help Desk at: 443-757-5802

National Aeronautics and
Space Administration
IS20
George C. Marshall Space Flight Center
Marshall Space Flight Center, Alabama
35812